

5 Abstract

~~This study analyzes turbulent properties in, and the thermodynamic structure-~~

Evaluation of methods to determine the surface mixing layer height of the atmospheric boundary layer in the central Arctic during polar night in cloudless and cloudy conditions

Elisa F. Akansu¹, Sandro Dahlke², Holger Siebert¹, and Manfred Wendisch³

¹Leibniz Institute for Tropospheric Research (TROPOS), Leipzig, Germany

²Alfred Wegener Institute (AWI), Helmholtz Centre for Polar and Marine Research, Potsdam, Germany

³Leipzig Institute for Meteorology (LIM), Leipzig University, Leipzig, Germany

Correspondence: Elisa F. Akansu (akansu@tropos.de)

Abstract. This study evaluates methods to derive the surface mixing layer (SML) height of the Arctic atmospheric boundary layer (ABL) using in situ measurements inside the Arctic ABL during winter and the transition period to spring. ~~These processes influence the evolution and longevity of clouds, and impact the surface radiative energy budget in the Arctic. For the~~
10 ~~measurements we have used an~~ An instrumental payload carried by a ~~helium filled tethered balloon~~. ~~This system was deployed~~
tethered balloon was used for the measurements between December 2019 and May 2020 during the yearlong Multidisciplinary drifting Observatory for the Study of Arctic Climate (MOSAIC) expedition. Vertically highly resolved ~~in-situ measurements of~~
profiles of (cm-scale) in situ profile measurements of mean and turbulent parameters were obtained, reaching from the sea ice
up to several hundred meters height. ~~The two typical states of the Arctic ABL above ground.~~

15 Two typical conditions of Arctic ABL over sea ice were identified: cloudless situations with a shallow ~~and stable ABL,~~
surface-based inversion and cloudy conditions ~~maintaining a mixed ABL. We have used with an elevated inversion. Both~~
conditions are associated with significantly different SML heights whose determination as accurately as possible is of great
importance for many applications. We used the measured turbulence profile data to ~~estimate the height of the surface mixing~~
layer. For this purpose, a bulk Richardson number criterion approach was introduced. By deriving a define a reference of the
20 SML height. With this reference, a more precise critical bulk Richardson number ~~for wintertime in high latitudes, we have~~
extended the analysis to radiosonde data. ~~of 0.12 was derived, which allows an extension of the SML height determination to~~
regular radio-soundings.

Furthermore, we have tested the applicability of the Monin-Obukhov similarity theory to derive ~~surface mixing layer~~ SML heights based on measured turbulent surface fluxes.

~~The Arctic climate is changing rapidly and the complex Arctic climate system is sensitive to multiple intertwined mechanisms. The applicability of the different approaches and their advantages and disadvantages are discussed.~~

1 Introduction

Currently, the Arctic climate is changing rapidly driven by intertwined mechanisms and feedbacks leading to an increased
 30 ~~near-surface near-surface~~ air temperature, sea ice retreat, and further significant changes ~~of in~~ Arctic climate parameters
 (~~Serreze and Barry, 2011~~)(Serreze and Barry, 2011; Wendisch et al., 2023a). Atmospheric and cloud processes ~~play an important~~
~~role in understanding the currently contribute significantly to these~~ ongoing climate changes in the Arctic (Wendisch et al.,
 2019). The enhanced response of the Arctic climate system to global warming is referred to as Arctic amplification. ~~It includes~~
~~feedback mechanisms, impacting factors, and sensitivity of the Arctic climate system.~~ There are still significant gaps in
 35 understanding this phenomenon ~~and uncertainties in modelling the driving processes (Wendisch et al., 2023a)~~causing major
~~uncertainties in projections of the future Arctic climate (Cohen et al., 2020).~~ In particular, the processes determining the evolu-
 tion of the Arctic atmospheric boundary layer (ABL) in cloudless and cloudy situations are not well ~~characterized and~~
~~represented by represented by weather/climate~~ models (Wendisch et al., 2019). The ABL is the atmospheric layer above the
 Earth's surface whose effects are perceptible on small time scales (up to several hours) and refers to the region of the atmo-
 40 sphere that is directly influenced by the surface (~~?Garratt, 1997~~)(Stull, 1988; Garratt, 1997). Especially during polar night, the
 vertical ~~extend extent~~ of the ABL plays an important role as stable stratification hampers the vertical exchange ~~of energy~~ and
 leads to a near surface warming contributing to Arctic amplification mostly in ~~the~~ winter (Graversen et al., 2008; Bintanja et al.,
 2011). Models often fail in reproducing shallow ABLs in the Arctic (Esau and Zilitinkevich, 2010; Lüpkes et al., 2010).

To advance our knowledge on ~~turbulent processes within the vertical structure of~~ the ABL, tethered ~~balloon-borne balloon-borne~~
 45 observations were performed during the yearlong Multidisciplinary Drifting Observatory for the Study of Arctic Climate
 (MOSAIC) expedition from September 2019 to October 2020 (Shupe et al., 2022). Profiling the lower atmosphere with ~~an~~
~~instrumental system carried by~~ a tethered balloon ~~system~~ provides high resolution ~~(125 Hz)~~ in situ data throughout the ABL
 reaching from the sea ice surface up to several hundred meters height ~~. Those observations enable an in-depth analysis of the~~
~~Arctic ABL during winter and spring above ground.~~

~~In the Arctic, the~~ The Arctic ABL is formed under unique conditions ~~such as, such as strong cooling of the~~ sea ice
 50 surface and the lack of solar radiation during winter, which ~~favor favors~~ the evolution of stable atmospheric ~~stratification~~
~~layering~~ (Persson et al., 2002; Tjernström and Graversen, 2009; Morrison et al., 2012; Brooks et al., 2017). Within this
 study, we refer to two ~~extreme conditions typical typical states~~ of the Arctic ABL ~~observed over sea ice~~ in winter: a cloud-
 less ~~boundary layer with a surface-based ABL with a surface-based~~ temperature inversion, and a cloudy ~~boundary layer~~
 55 ~~ABL~~ with a pronounced cloud top inversion (~~Tjernström and Graversen, 2009; Stramler et al., 2011; Morrison et al., 2012).~~
 (~~Tjernström and Graversen, 2009; Stramler et al., 2011; Morrison et al., 2012; Wendisch et al., 2023b).~~ We have distinguished

between those two states of the atmosphere, as many models have difficulties to reproduce the bimodal distribution of the terrestrial radiation (Solomon et al., 2023).

Under cloudless conditions, the atmosphere cools radiatively from the surface (strong negative thermal-infrared net irradiances), forming a surface based temperature inversion leading to a stably stratified lower atmosphere. Due to shear stress, ~~the main~~ which comprises a major source of turbulence in the Arctic ABL, a surface mixing layer (SML) can evolve even though stability dampens turbulence (Brooks et al., 2017). The SML ~~is~~ relates to the lowermost part of the atmosphere that is turbulent ~~or at least intermittently turbulent~~, however, the SML height¹ does not necessarily equal the ABL height, because disconnected turbulence may occur aloft (Grachev et al., 2013). If clouds form, the ~~surface-based~~ surface-based temperature inversion is lifted upward to the cloud top. ~~In~~ Then, in addition to mechanically induced turbulence at the surface, a second source ~~for of~~ turbulence at cloud top ~~exists due to negative buoyancy, which finally evolves caused by negative buoyancy due to~~ radiatively cooled air at cloud top, which leads to a cloud mixed layer (Tjernström and Graversen, 2009; Morrison et al., 2012). Especially ~~low-level Arctic clouds~~, low-level Arctic clouds impact the surface radiative energy budget (Intrieri et al., 2002a; Shupe and Intrieri, 2004) and thus alter the vertical structure of the ABL (Tjernström and Graversen, 2009). ~~The~~ Furthermore, the vertical stratification of the ABL influences the formation and longevity of clouds (Intrieri et al., 2002a; Sedlar and Tjernström, 2009; Shupe et al., 2013; Turner et al., 2018) as, for example, surface sources of atmospheric moisture, energy and cloud forming particles ~~are assumed to~~ have a significant impact on cloud properties (Gierens et al., 2020; Griesche et al., 2021). While cloudless conditions are rather scarce in the Arctic (Intrieri et al., 2002b), ~~clouds and their influence become even more important~~ frequently occurring low-level mixed-phase clouds are of major importance for the surface radiative energy budget.

Furthermore, local ~~boundary layer~~ ABL processes might be ~~overlaid~~ influenced by advection of warmer/cooler air masses ~~at certain altitudes~~. As a result, elevated inversions can form ~~above the lowermost atmospheric layer~~ which decouple different layers. These elevated inversions would not meet the classical definition of the ABL, although they may ~~well~~ feedback to the air layer near the surface ~~(?)~~ (Mayfield and Fochesatto, 2013). Between the two typical radiative states (cloudless and cloudy), the ABL alternates on the time scale of hours, ~~but the exact time scale has~~ although they have not yet been investigated in detail, mostly because corresponding ~~temporally high-resolution~~ high-resolution profile measurements are missing.

Further ~~questions~~ issues regarding the turbulent properties and thermodynamic structure of the Arctic ABL in winter include, for example, the heights up to which ~~height~~ heat energy is distributed or aerosol particles are mixed from the surface. Therefore, the determination of the SML height ² ~~is ultimately important.~~

is of utmost importance. Widely used approaches to determine the height of the SML are based on observed thermodynamic profiles. An overview of common identification methods can be found in Vickers and Mahrt (2004), Dai et al. (2014), and Jozef et al. (2022). The definition of the top of the SML is not always straight forward; in particular, it becomes even more complex as the criteria are not very pronounced for stable stratification ~~(Mahrt, 1981; ?)~~ (Mahrt, 1981; Stull, 1988). The basic idea behind the definition of a SML height is that starting from the surface, a property or matter is mixed upwards by turbulence, and this mixing is terminated when the turbulence is no longer strong enough for vertical mixing. An obvious definition of the

¹ In the following parts of this study we avoid the rather general term ABL height and use the term SML height for our analysis.

² ~~We avoid the rather general term ABL height and use the term SML height for our analysis.~~

90 SML height h is, therefore, based on the vertical distribution of a suitable turbulence parameter and a threshold, which, if below this value, defines the SML height (Dai et al., 2014). Here we use direct ~~balloon-borne~~ balloon-borne turbulence observations, in particular, energy dissipation rate ε profiles, to estimate the SML height ~~, which is defined as the height where turbulence ceases~~ (Balsley et al., 2006). By observing turbulence by in situ measurements, the SML height can be ~~either defined~~ derived directly. One can either define the SML height as the height where ε drops significantly with height, or when the flow is
95 considered ~~non-turbulent~~ non-turbulent based on a "turbulence threshold" (Shupe et al., 2013; Brooks et al., 2017).

~~Other widely used approaches to determine the depth of the SML are based on observed thermodynamic profiles. An overview of common identification methods can be found in Dai et al. (2014) and Jozef et al. (2022). One~~ Another approach to define the SML height applies the bulk Richardson number Ri_b (Andreas et al., 2000; Dai et al., 2014; Zhang et al., 2014; Zilitinkevich and
~~The bulk Richardson number allows the derivation of the equilibrium~~ (Andreas et al., 2000; Zilitinkevich and Baklanov, 2002; Dai et al., 2002).
100 Ri_b is derived from the ratio between shear and buoyancy and is a measure of whether turbulence tends to increase or decrease. The SML height is defined by the height where turbulence ~~decays and from that to estimate the SML height based on~~ can not be sustained because the bulk Richardson number exceeds a critical value (Zilitinkevich and Baklanov, 2002; Andreas et al., 2000).
~~It should be explicitly emphasised that this approach can also be applied to a stably stratified atmosphere. The turbulence based SML heights are used of~~ Ri_b (Zilitinkevich and Baklanov, 2002; Andreas et al., 2000). This critical value, however, is under
105 discussion and varies, for example, among sites (Vickers and Mahrt, 2004).

We use the turbulence-based SML heights as reference to derive a critical bulk Richardson number for the ~~wintertime and winter and spring~~. The in situ turbulence perspective not only allows to derive a critical value but also to evaluate the bulk Richardson number approach. It should be emphasised that this approach can also be applied to a stably stratified atmosphere. Further, continuous ~~surface-based~~, surface-based energy flux measurements can be used to estimate the SML height using Monin-Obukhov similarity theory (Zilitinkevich, 1972; Vickers and Mahrt, 2004). The Monin-Obukhov similarity theory describes the near-surface turbulent exchange processes based on surface measurements. This approach can complement the balloon-borne SML height estimates between balloon launches.

The current study discusses ~~the observed profile measurements and the instrumental setup. Typical Arctic boundary layer properties and the of Arctic ABL turbulent properties and related~~ effects of clouds on the vertical ~~structure are discussed,~~ approaches for SML height estimation for the thermodynamic structure. The data are used to develop a new, more accurate approach to estimate the SML height in Arctic winter and spring ~~are examined~~. To investigate possible SML height criteria, the in situ energy dissipation rates are compared to bulk Richardson number profiles and a surface ~~flux-based~~ flux-based method. Furthermore, we apply ~~this critical value to the critical~~ Ri_b value technique for deriving the SML height ~~estimation~~ using both tethered balloon as well as radiosonde data.

2.1 Observations in ~~the winter and spring seasons~~ during the MOSAiC expedition

During the MOSAiC expedition, the research vessel (RV) *Polarstern* (Knust, 2017) was frozen to an ice floe ~~following the Polar drift~~ drifting from October 2019 until September 2020. ~~This The MOSAiC expedition~~ facilitated measurements onboard RV *Polarstern* and on the ice floe in different fields throughout an entire seasonal cycle. An overview of the atmospheric measurements is given by Shupe et al. (2022), ~~and~~ information about the sea ice and ~~oceanography aspects are~~ oceanographic aspects is summarized by Nicolaus et al. (2022) and Rabe et al. (2022). Figure 1a shows the course of the drift of ~~the ship~~ RV *Polarstern* in winter and spring when the ~~helium-filled~~ tethered balloon *Miss Piggy* (Becker et al., 2020) was deployed from the ice floe close to RV *Polarstern*. A detailed view ~~on of~~ the temporal evolution and the balloon flight days is given in Fig. 1b. The balloon ~~was filled with helium~~, has a volume of about 9 m^3 , and allows to lift a modular scientific payload of up to 4 kg (Becker et al., 2020). ~~The setup enables continuously. The tethered balloon enables continuous~~ vertical profiling of the lowermost 1.5 km of the atmosphere with a climbing rate of ~~around 1 to 2~~ m s^{-1} . Measurements can be performed ~~during day and night as well as under cloudy conditions with light icing. The deployment of the balloon is limited by weather conditions, such as strong winds inhibited by strong winds (wind velocity above about 7 m s⁻¹ at the surface) or precipitation associated with severe icing. Thus, weather-related selective sampling occurred and Therefore, weather-related selective sampling~~ should be considered for further interpretation.

~~The data used in this work were measured with a hot wire~~ A hot-wire anemometer package specifically designed for turbulence observations (Egerer et al., 2019) ~~drifting, hereafter referred to as "turbulence probe", was used to measure the data of this study. Data were collected when the ice floe drifted~~ between $86.14^\circ\text{ N } 122.21^\circ\text{ E}$ and $83.92^\circ\text{ N } 17.69^\circ\text{ E}$ between 6 December 2019 and 6 May 2020 (Fig. 1b). The ~~entire data set and its processing is described by Akansu et al. (2023a). The~~ instrument is attached to a tether about 10 m ~~to 20 m~~ below the balloon to minimize flow distortions induced by the balloon. ~~The system is mounted movably. In addition, the instrument package attached to the balloon tether is mounted flexibly, it is~~ aligned horizontally and equipped with a tail to keep the setup into the mean flow direction. The instrument consists of ~~an one-component a~~ hot wire anemometer to measure wind velocity ~~with 125 Hz temporal resolution, and a thermocouple for air temperature observations with 125 measurements with 10 Hz temporal resolution. Besides the high-frequency high-frequency records, 1 Hz~~ measurements of wind velocity based on a Pitot static tube ~~are available accompanied by have been made and~~ basic measurements of static pressure, temperature, and relative ~~air~~ humidity. Due to weather conditions, the Pitot tube, which served as a reference for hot wire calibration, was frequently affected by icing. Therefore, a standard meteorology tethersonde, which ~~is part of belongs to~~ the modular balloon equipment and ~~separated approximately 5 is separated about 10 m~~ from the turbulence probe, ~~served as was the~~ mean reference for the fast sensors. The turbulence probe was deployed on 34 days ~~reaching, sampling~~ the height range from the surface ~~up to typically a few hundreds meters. hundred meters.~~ After quality control, ~~88-99~~ individual vertical profiles (ascents and descents) ~~are available have been provided~~ for further analysis. ~~Figure In this study, 81 out of the 99 profiles are used because not all measurements reach to the surface, and some contain error-prone temperature data.~~

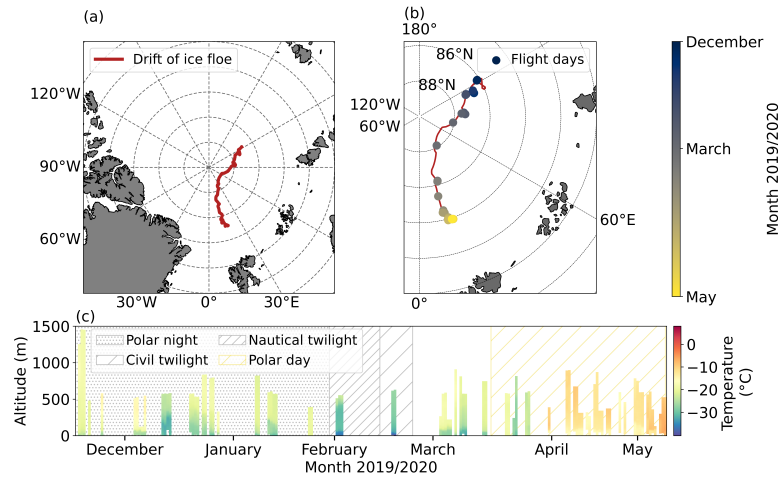


Figure 1. Overview of [the drift of the ice floe during](#) tethered balloon [borne-operations in winter and spring](#) (a), and [daylight conditions](#) and location of the days with balloon operations (b). Temperature measurements [of all profiles are shown in](#) (c). The background shading indicates the respective daylight conditions during the observation period.

[Figure 1c](#) displays an overview of all temperature profiles, the respective maximum height and daylight conditions. [Table A1](#) shows all profiles and their launch times.

155 Continuous, [near-surface](#) observations of meteorological and turbulence parameters were performed at a location on the ice floe called *Met City* (Shupe et al., 2022). Measurements with an ultrasonic anemometer/thermometer were taken at a meteorological tower [in-at](#) 2 m, 6 m, and 10 m [height-heights](#) serving as surface reference for our balloon observations. Furthermore, the [net-irradiancees](#) [upward](#) (\uparrow) and [downward](#) (\downarrow), broadband terrestrial irradiances F (in units of W m^{-2}) were collected at the [Atmospheric Surface Flux Station with a Precision Infrared Radiometer](#) (Shupe et al., 2022). The net irradiances $F_{\text{net}} = F^{\downarrow} -$
160 F^{\uparrow} are taken as a proxy for the radiative energy budget at the surface. [Furthermore, the measurements at Met City include the surface radiometric skin temperature.](#)

Regular radiosondes were launched every six hours (5, 11, 17, and 23 UTC) from the helicopter deck of RV *Polarstern* (12 m above mean sea level) providing information on the [dynamic and](#) thermodynamic structure of the atmosphere. It should be noted ~~,however,~~ that the data obtained within the first tens of meters can be influenced by the ship itself and should therefore
165 be interpreted with caution. The ship can create flow distortions and can serve as a heat island, but also radiosonde data near the surface are often still subject to errors. Especially the wind determined by GPS ([Global Positioning System](#)) data might be influenced by the unwinding of the probe from the tether (~~?Jozef et al., 2022~~)([Achtert et al., 2015; Jozef et al., 2022](#)). To compare the radiosonde ~~to-and~~ the tethered balloon [profiles](#)[profile measurements](#), the corresponding radiosonde [measurements](#) [data](#) are selected with launch times closest to the tethered balloon flight. The time difference between both launches is at
170 most around 3 hours. However, the atmospheric structure may change within a few hours or even less. ~~The evolution of the atmosphere has to be considered when comparing the respective launches.~~

In-situ measurements are complemented by Cloudnet retrievals to characterize the cloud situation (Hlingworth et al., 2007; Griesche et al., 2020). The cloudy Arctic ABL can be very shallow, especially in winter, and hence poses challenges on remote sensing approaches to detect the very low cloud layers (Griesche et al., 2020). For the question of the influence of clouds on the ABL dynamics, however, the net ~~radiation is of~~ irradiances are of main importance, which ~~is~~ are directly influenced by the clouds. Therefore, the ~~net radiation~~ (terrestrial net radiation F_{net}) measurements at Met City, where F_{net} is the cumulative surface radiative flux irradiance, are used as an independent "cloud indicator". Cloudless conditions prevail when the net radiation is below -25 W m^{-2} , while higher values are associated with clouds (Wendisch et al., 2023a). To avoid ambiguous allocations, data with net radiation in the range between -28 W m^{-2} and -22 W m^{-2} are not considered. Additionally, the cloud condition was manually compared with 360° photographs and all sky total imager observations (as far as possible regarding daylight conditions).

2.2 Estimation of the surface mixing layer height

The determination of the SML height can be done in different ways depending on the type of measurements available. A comprehensive overview of the different methods is given by Vickers and Mahrt (2004). Here we focus mainly on the advantage of high-resolution profile measurements using the tethered balloon. Thus, we first

In this chapter, we present several methods for determining SML heights based on different available data sets. First, we discuss a method to derive SML heights that benefits directly from local turbulence measurements and then, serves will serve as a reference for a method based on mean profiles other approaches in the following (Sect. 2.2.1). A second method is based on the mean temperature and wind speed profiles in the context of the bulk Richardson number criterion (Sect. 2.2.2). Finally, we compare the results with a method based on surface flux observations, previous results with SML heights based on the application of the Monin-Obukhov similarity theory and thus on the determination of surface fluxes (Sect. 2.2.3).

2.2.1 In-situ turbulence method

2.2.1 Direct in situ method

The basic idea behind the definition of a SML height is that starting from the surface, a property or matter is mixed by turbulence upwards, and this mixing is terminated when the turbulence is no longer strong enough for vertical mixing. An obvious definition of the SML height h is, therefore, The direct in situ method for estimating the SML is based on the vertical distribution of a suitable turbulence parameter and a threshold, which, if below this value, defines the SML height (Dai et al., 2014).

assumption that the turbulence at the top of this layer falls below a certain threshold, indicating the transition from a turbulent to a comparatively laminar layer. For our application, we chose the energy dissipation rate ε as turbulence measure to quantify turbulence because it can be determined as a local parameter from short temporal subsections during a balloon ascent. Based on Kolmogorov's inertial subrange theory, ε can be estimated in different ways (Wyngaard, 2012). A comparatively robust and proven method has been found to determine ε using the second-order structure function (Siebert et al., 2006, and references therein).

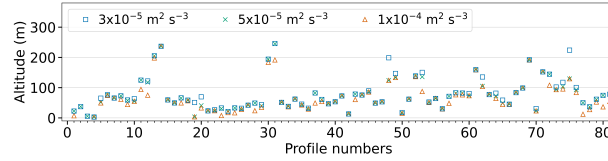


Figure 2. ~~Turbulence-based SML~~ Surface mixing layer heights derived from direct turbulence measurements for each profile. Three thresholds separate turbulent and non-turbulent flows: $1 \times 10^{-4} \text{ m}^2 \text{ s}^{-3}$, $5 \times 10^{-5} \text{ m}^2 \text{ s}^{-3}$, and $3 \times 10^{-5} \text{ m}^2 \text{ s}^{-3}$.

(Siebert et al., 2006):

$$S^{(2)}(\tau) = \left\langle (u(t+\tau) - u(t))^2 \right\rangle = 2(\varepsilon \cdot U \cdot \tau)^{2/3}, \quad (1)$$

205 with $u(t)$ being the longitudinal wind velocity component as measured at time t . The averaging in Eq. (1) denoted by the rectangular-angle brackets is performed over all t , so the structure function $S^{(2)}$ is a function of time lag τ which has been calculated by applying Taylor hypothesis (s frozen turbulence hypothesis (transferring time lag to spatial increment $r = U \cdot \tau$) with the mean flow velocity U (see Stull (1988) for more details). It has been shown by Frehlich et al. (2003) that 100 samples are sufficient in order to provide robust estimates of local ε . Here, we use an integration over 125 samples (e.g., 1 s) resulting
210 in a vertical resolution of roughly 1 to 2 m.

~~Therefore, profiles~~ Profiles of ε allow direct identification of the SML height, denoted hereafter as h_ε . This method has the disadvantage that there is no physically unambiguous definition of the limit value for ε and ~~therefore~~, ~~therefore~~, different values are used in the literature (Shupe et al., 2013; Brooks et al., 2017), which are close to each other. We tested three values to estimate h_ε that ~~previously~~ have been used ~~previously~~: $1 \times 10^{-4} \text{ m}^2 \text{ s}^{-3}$, $5 \times 10^{-5} \text{ m}^2 \text{ s}^{-3}$ and $3 \times 10^{-5} \text{ m}^2 \text{ s}^{-3}$. We consider the
215 SML to be constrained when ε falls below the threshold for at least 10 consecutive levels, while the h_ε equals the lowermost of those levels. These 10 ~~consecutive levels~~ levels ensure that the turbulent layer and non-turbulent layer are well separated.

Figure 2 shows the ~~different~~ estimates of h_ε for each profile ~~depending on~~ for the different thresholds. The profile numbers refer to the profiles used in this study. An overview is given in Table A1. Although the highest threshold almost always results in yields the lowest h_ε values, the variations for the different thresholds vary considerably from profile to profile. However, the
220 two lowest thresholds are very close to each other and result in almost identical nearly identical values of h_ε . To identify the appropriate threshold value, we have manually examined the examined all thermodynamic profiles and the profiles of the ε . As a result we have decided on the threshold value of $\varepsilon = 3 \times 10^{-5} \text{ m}^2 \text{ s}^{-3}$.

2.2.2 Bulk Richardson number method

The turbulent state of an atmospheric layer can be analyzed using the (gradient) Richardson number Ri_{g} , which describes the
225 relationship between thermodynamic stability and turbulence-producing wind shear (e.g., ?): turbulence-producing horizontal

wind shear (e.g., Stull, 1988):

$$Ri_g(z) = \frac{\frac{g}{\theta} \frac{\partial \theta}{\partial z}}{\left(\frac{\partial u}{\partial z}\right)^2 + \left(\frac{\partial v}{\partial z}\right)^2}, \quad (2)$$

with the potential temperature of dry air θ , the horizontal wind components u and v (zonal and meridional, respectively), and $g = 9.81 \text{ m s}^{-2}$, and z as height above ground. This stability measure describes whether there is a tendency for turbulence to weaken or strengthen, usually, a theoretical value of 0.25 is assumed at which the tendency turns. Therefore, Ri_g profiles can be used to derive the equilibrium height at which turbulence decays, which coincides with the SML height h_{Ri_g} (Zilitinkevich and Baklanov, 2002; Andreas et al., 2000). However, the practical use of the gradient Ri_g is somewhat limited because the calculation of mean gradients (temperature and wind speed) (local wind and temperature gradients) based on observational data is often subject to uncertainties that lead to large variations in the Ri_g profiles, and scatter in the Ri_g profiles. In particular, the necessary filtering leads to further ambiguities. For this reason, modified definitions for Ri_g have been derived, which offer advantages, especially for observational data. An alternative Ri number is the so-called surface bulk Richardson number Ri_b (Mahrt, 1981; Andreas et al., 2000; Heinemann and Rose, 1990), whose definition is not based on the explicit calculation of local gradients, but includes the complete layer from the ground surface to the current measurement height z :

$$\left(\overline{U(z)}\right)^2,$$

(3)

with the numerator as the buoyancy term where θ_0 is the potential temperature of dry air at the surface level, and $\Delta\theta = \theta(z) - \theta_0$ is the temperature difference between the potential temperatures at the current height z and surface and z . According to the basic concept of the surface bulk Richardson number approach, the surface level, lower reference level is the surface where the mean horizontal wind velocity equals zero $U(z = z_0)$ and g is the gravitational acceleration. $U(z)$ is the horizontal wind speed at height z indicating the bulk shear. For surface temperature, we use observations at the skin temperature. Since other studies are often based on radiosonde observations only, the temperature at 2 m is then typically used for θ_0 , even though this value may differ from the skin temperature, especially for stably stratified conditions with strong surface temperature gradients. To be consistent with other studies, we first use temperature observations at 2 m height of from the Met City tower, because the balloon-borne temperature readings are not completely reliable within the lowest meters. Surface bulk Richardson numbers are calculated for each altitude z of the profile with the surface as lower level assuming that the wind velocity at the surface vanishes for θ_0 . Then, for comparison, the same analysis is performed using the skin temperature measured during MOSAiC.

Compared to other bulk Ri -definitions, where mean gradients are estimated for distinct layers of δz (Jozef et al., 2022), the surface $Ri_{\delta z = 30 \text{ m}}$ (Jozef et al., 2022), for example, the Ri_b -approach applied here fails if multiple turbulent layers are

present. However, as we want to estimate the height of the SML, ~~detecting~~ only the lowermost continuous turbulent layer ~~is needed-needs to be detected~~, and the surface approach with an increasing layer depth is sufficient. Furthermore, ~~looking at from the values of h_ε presented~~ in Fig. 2, it ~~is-becomes~~ apparent that the majority of the SML heights ~~lies-lie~~ within the lowermost
260 100 m, many even do not exceed 50 m altitude and ~~multi-multiple~~ turbulence layers are rare.

The height of the SML h_{Ri_b} ~~can be defined as the altitude where a critical value of the~~ is the height at which the surface bulk Richardson number Ri_b ~~is reached-and-reaches a critical value and the~~ turbulence decays. The top of the SML is, ~~thus~~, the highest level where $Ri_b < Ri_{bc}$. ~~The-However, the~~ definition of Ri_{bc} is ~~,-however,-~~ not straightforward and ~~a variety of Ri_{bc} values can be found in literature (e.g., Zilitinkevich and Baklanov, 2002)not based on a theoretical concept~~. It appears
265 that the differences for Ri_{bc} measured at different sites are larger than the variation within an observation period at a fixed site (Vickers and Mahrt, 2004)~~and the "theoretical value" of Ri_{bc} =~~. When applying 0.25 overestimates as a critical value for the bulk approach, the experimentally determined ~~values-SML heights are overestimated~~ (Brooks et al., 2017). However, ~~it must be taken into account that the theoretical this theoretical critical value was derived for the gradient Ri number and , therefore, it is Ri_g number and is therefore~~ not directly applicable to the surface bulk approach. ~~However, by comparison with~~ In addition,
270 Eq. (3) is sensitive to the lowest observation level, which may also explain some of the variation in Ri_{bc} . However, using the "reference" SML height h_ε introduced in subsection 2.2.1 Ri_{bc} can be estimated (see Sect. 2.2.1, we can provide a direct and robust estimate for Ri_{bc} (see Sect. 3.3).

2.2.3 Surface ~~flux-based~~ flux-based method ~~If surface fluxes dominate~~

If surface energy fluxes are the main drivers for the development of a SML, ~~the height h_{sr} should be it is proposed that the SML~~
275 height is a function of the Monin-Obukhov length L (Vickers and Mahrt, 2004):

$$L = -\frac{u_\star^3}{B_s} \frac{u_\star^3}{B_s}, \quad (4)$$

with ~~$B_s = gT_0^{-1}\langle w'T' \rangle$ being the normalized~~ $B_s = g \cdot T_0^{-1} \langle w' \cdot T' \rangle$ being the surface buoyancy flux and ~~$u_\star^2 = -\langle u'w' \rangle$~~ $u_\star^2 = -\langle u' \cdot w' \rangle$ being the friction velocity. Besides more simple relationships ~~($h_{sr} \propto L, ?$), ? (e.g., $h \propto L$, Kitaigorodskii, 1960)~~, Zilitinkevich (1972) proposed a formulation including the Earth's rotation:

$$280 \quad h_{sfMO} = C_{sr} \sqrt{\frac{u_\star L}{f}}, \quad (5)$$

with ~~C_{sr}~~ C being a scaling constant of $\mathcal{O}(1)$ and the Coriolis parameter f . All parameters included in Eq. (5) ~~have been were~~ calculated continuously using ultrasonic anemometer readings at the *Met City* tower. With the Monin-Obukhov scaling method, referred to as the MO method hereafter, the SML height can be derived continuously and complements balloon-borne SML height estimates. However, Eq. (5) is only valid for stable stratification ($B_s < 0$ and $L > 0$), and the method fails if further
285 sources ~~for-of~~ turbulence are present at higher levels (such as clouds or Low-Level Jets (LLJs)). Again, the in situ turbulence method is helpful to assess the applicability of the MO method (Sect. 3.5).

3 Results and discussion

3.1 Two contrasting states of the Arctic wintertime ABL: ~~surface-based~~ Surface-based versus elevated inversion

In the introduction (Sect. 1), ~~it was~~, we have argued that the Arctic winter ABL ~~alternates between two~~ mainly alternates
290 between cloudless and cloudy conditions. We begin at this point by illustrating these two typical conditions ~~with the help~~
~~of presenting two~~ examples. The first case represents a cloudless ABL with a pronounced surface inversion, and the second
case describes a cloudy ABL and the resulting elevated inversion at the cloud top with a ~~less well-mixed, neutrally stratified~~
well-mixed layer below the inversion. Figure 3 shows the two example measurements of potential temperature θ , horizontal
wind velocity U , local energy dissipation rate ε , and surface bulk Richardson number Ri_b as a function of altitude. Cloudless
295 conditions prevailed during a profile observed on 5 March 2020 with a strong ~~surface-based~~ surface-based temperature inversion
($\Delta\theta \approx 6$ ~~$\Delta\theta \approx 7$~~ K within about 40 m) up to 50 m followed by a ~~slightly less~~ stably stratified layer above (Fig. 3a). ~~Near the~~
~~surface, the wind speed~~ The wind velocity U increases with height ~~, peaking at from the surface up to a height of~~
50 ~~magain and continuing almost constantly until~~, and then remains almost constant up to the maximum height of the profile
(Fig. 3b). The strongest increase in ~~wind speed~~ U is in the lowest altitude layers up to about 30 m, ~~in~~ the region with the
300 ~~strongest~~ highest turbulence in terms of ε (Fig. 3c). Above 30 m, the turbulence decreases rapidly by two to three orders of
magnitude and according to the threshold, as defined in Sect. 2.2.1, the upper limit of the SML height is reached here.

The surface bulk Richardson number (Fig. 3d) ~~almost linearly increases~~ increases almost linearly with height for the cloud-
less conditions.

The example for the vertical stratification under cloudy conditions, as measured on 29 December 2019 ~~indicates~~, shows an
305 elevated inversion with its base at around 220 m, indicating cloud top. A ~~well-mixed~~ well-mixed layer prevails below the
inversion ~~with the wind speed~~, with U gradually increasing from the surface to the inversion base from 6 m s^{-1} to 9 m s^{-1} .
Clearly, the turbulence reaches from the surface up to ~~around about~~ 240 m height ~~where it~~, where ε rapidly drops below the
threshold ~~indicating the height of the SML~~, indicating the SML height. The extent of the ~~mixing layer~~ SML is also clearly
visible in the Ri_b profile (Fig. 3d). The surface bulk Richardson number ~~is almost constant in~~ remains almost constant with
310 height in this region with values close to zero ~~and starts to significantly grow~~, it starts to increase significantly only at the
inversion base height, exactly where ε starts to decrease ~~almost quite~~ abruptly and the upper limit of the SML height is reached.

3.2 Vertical mean and turbulent structure of the ABL

To ~~obtain the typical~~ illustrate the main features of the mean temperature stratification for the two typical situations, we
315 ~~normalize all measured profiles and~~, plot and average ~~them all measured profiles~~ (Fig. 4), ~~distinguished~~ distinguishing between
surface (Fig. 4a) and elevated (Fig. 4b) inversions. The height is normalized by h_ε , and the temperature is shifted by the surface
value θ_0 and normalized by the inversion strength ~~($\Delta\theta = \theta(h_\varepsilon) - \theta_0$)~~ $[\Delta\theta = \theta(h_\varepsilon) - \theta_0]$, so that the normalized temperature in
the SML height takes the value one. A similar plot ~~for including~~ the contrasting summertime Arctic can be found in Tjernström
and Graversen (2009).

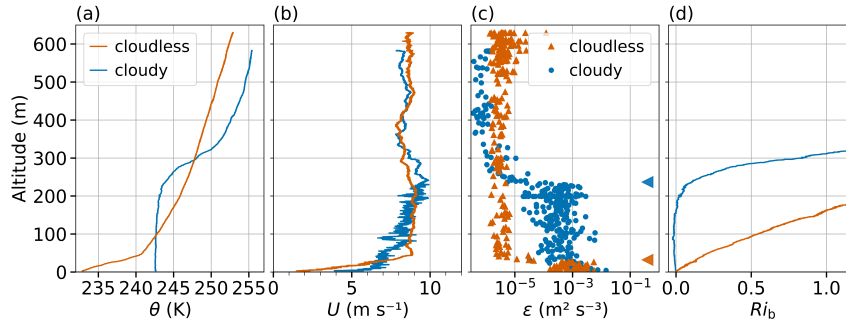


Figure 3. Tethered ~~balloon-borne~~ balloon-borne profiles obtained under cloudless conditions (orange) on 5 March 2020, 12:27 UTC, and under cloudy conditions (blue) on 29 December 2019, 11:55 UTC. Panel (a) shows the profiles of potential temperature over height, (b) the wind velocity, (c) the derived energy dissipation rates and (d) the bulk Richardson number. The SML heights for cloudless (orange) and cloudy conditions (blue) derived by in situ turbulence records are indicated by left pointing triangles on the right in (c).

Due to operational constraints, not all profiles reach up to the same height but every launch exceeds, but all launches used here exceed 200 m altitude and, therefore, most of the profiles exceeds, and therefore most profiles exceed at least twice h_ϵ . The two averaged temperature profiles have quite different characteristics. While the profile is nearly linear from the ground surface to h_ϵ under for cloudless conditions, the well-mixed well-mixed sub cloud layer for the cloudy case provides shows a gradual increase in temperature to then rise, rising much more sharply when at h_ϵ is reached. As it, As is often observed in Arctic clouds, the temperature rise at increase at the inversion base already begins clearly inside the cloud; in this normalization, this normalization does not consider the cloud layer thickness is not included and, and hence, the temperature curve in Fig. 4b must be interpreted with caution. In addition, it must be emphasized that we do not present the liquid-water equivalent potential temperature, which under adiabatic conditions is also height constant within the cloud.

In Fig. Figure 5 shows the relative probability distribution of ϵ is shown using 5 m height intervals of all measured profiles. The turbulence distribution for surface-based surface-based inversions (Fig. 5a) shows, 30 profiles) shows the highest values near the surface (wind shear-driven shear-driven turbulence) and significantly low values lower ones above approximately 60 m height. Higher probabilities of ϵ at heights around 500 m height occurred during single events and might be related to Low-Level Jets (LLJ) LLJs. However, the observations are too sparse to draw conclusions about the occurrence of possible multi-layer multi-layer turbulent structures. For ABL structures with elevated inversions (Fig. 5b, 34 profiles), the turbulence is still highest in the lowermost tens of meters. But here, the turbulence continuously reaches up to around 200 m. The chosen threshold of $\epsilon = 3 \times 10^{-5} \text{ m}^2 \text{ s}^{-3}$ is used to distinguish turbulent and non-turbulent distinguishes turbulent and non-turbulent regions of the profiles. Using With this threshold approach, almost all observations above 200 300 m height for elevated inversions (60 m height for surface inversions) are considered as non-turbulent and, therefore, non-turbulent and thus well above the SML. In contrast to the summertime Arctic boundary-layer ABL, where Brooks et al. (2017) found two separated turbulence maxima indicating decoupling, we did not identify clearly pronounced turbulence layering and decoupling plays a minor role.

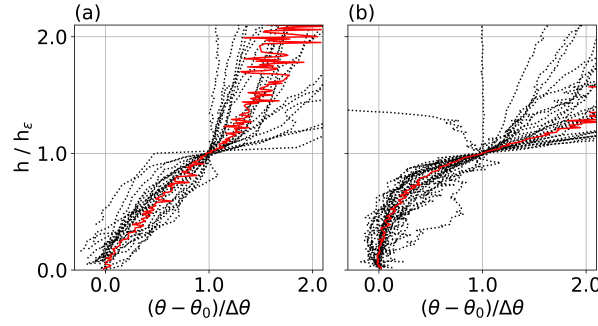


Figure 4. Normalized potential temperature profiles of tethered balloon borne measurements over height. All profiles are separated in respect to the inversion heights, such as surface based inversion (a) or elevated inversion (b). The height is normalized using the turbulence based SML height h_ϵ while the temperature is normalized using the potential temperature gradient of the SML and the potential temperature close to the surface.

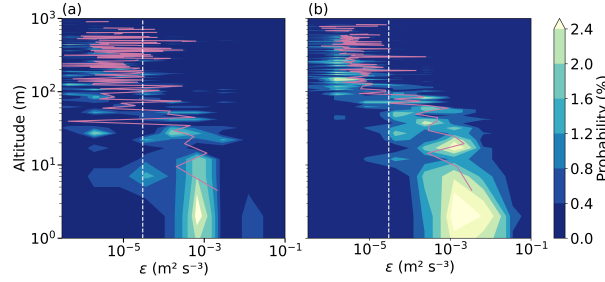


Figure 5. Probability of the energy dissipation rates as a function of height. The profiles are distinguished in respect to the temperature profile: (a) shows all profiles with surface based inversions and (b) profiles with elevated inversions. The probability of ϵ is calculated for 5 m height bins starting at a height of 2 m. To complement the data from the surface, the first bin reaches from the surface up to a height of 2 m. Additionally, the median (solid line) profile of ϵ (5 m bins starting at 2 m height) is given in purple. The turbulence threshold value of $3 \times 10^{-5} \text{ m}^2 \text{ s}^{-3}$ is depicted by the white vertical dashed line in both panels.

3.3 Estimating the critical Bulk Richardson Number

The estimation of Estimating the SML height based on the surface bulk Richardson number requires the definition of the a critical value Ri_{bc} . Here, we apply a method used by Vickers and Mahrt (2004) by plotting the buoyancy term versus against the shear term in Fig. 6 for all profiles at h_ϵ in Fig. 6. The slope of the linear fit is then equivalent corresponds to the critical surface bulk Richardson number Ri_{bc} . Based on a data set comprising 64 data from 80 profiles, we derive a critical value of $Ri_{bc} = 0.12$ which is about half of, about half the theoretical value of 0.25. As mentioned in Sect. 2.2.2, we would like to point

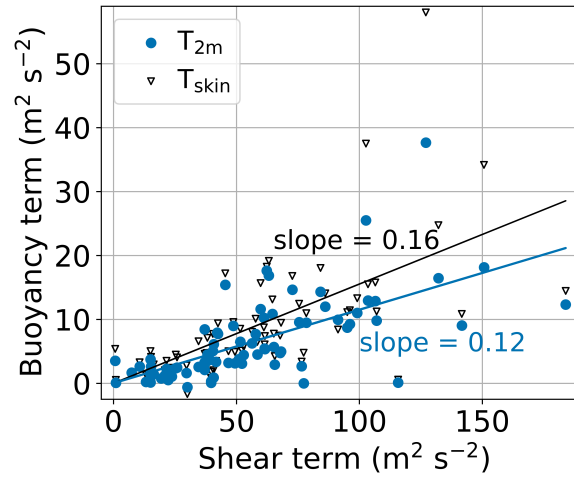


Figure 6. Buoyancy term versus shear term of the surface bulk Richardson number calculated according to Eq. 3 using the temperature at 2 m height T_{2m} (blue) and the skin temperature T_{skin} (black) as θ_0 . The solid line indicates the least squares fit that is forced through the origin. The critical bulk Richardson number Ri_{bc} is equivalent to the slope of the fit. The critical values are 0.12 for T_{2m} and 0.16 for T_{skin} .

out again that this "theoretical value" should be understood as an order of magnitude for the surface bulk Richardson number approach rather than a reference value.

Applying the same analysis with the skin temperature as θ_0 , we derive $Ri_{bc} = 0.16$ (Fig. 6). This difference shows clearly how strongly the derived value for Ri_{bc} depends on the selected surface reference. Furthermore, we can assume that the temperature measured at a height of 2 m on a mast is also significantly more accurate than a corresponding measurement with a radiosonde, which has comparatively large inaccuracies in the lower ranges.

In order to get

To obtain a rough measure for the robustness of the Ri_{bc} estimate, Fig. 7a–7 shows the frequency of occurrence of Ri_{bc} . Clearly, the majority of Ri_{bc} using the temperature at 2 m height as θ_0 is centered around the mean-critical value of 0.12 ± 0.04 , with a few outliers even exceeding the theoretical value. The frequency distribution of Ri_{bc} with T_{skin} as θ_0 is slightly shifted towards higher Ri_{bc} values.

As described by Vickers and Mahrt (2004), the critical bulk Richardson number varies not only between locations but also under different not only varies between sites but is also a function of atmospheric conditions (cloudless, cloudy). To understand which influence might may lead to different values of Ri_{bc} , the data are separated according to we distinguished the data by the cloud conditions because the radiative effect of clouds directly changes the turbulent fluxes at surface and thus the SML height. Figure 7b shows the distribution of using F_{net} . While we have derived Ri_{bc} for cloudless and cloudy conditions, respectively. Even though the frequency distribution of Ri_{bc} for cloudless conditions peaks at slightly higher values than for

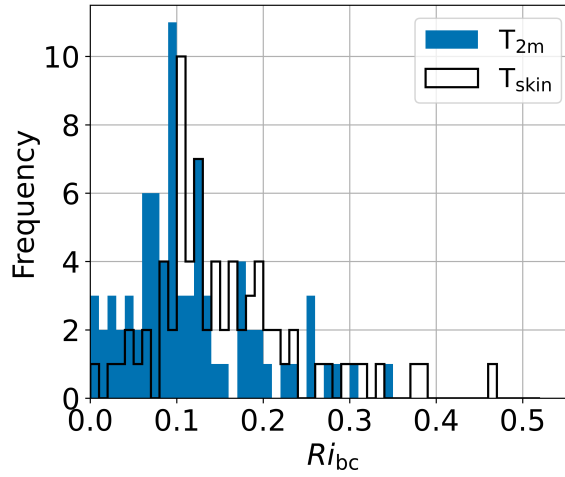


Figure 7. Frequency distributions of bulk Richardson numbers at the SML height h_ϵ using the temperature at 2 m height T_{2m} (blue) and the skin temperature T_{skin} (black) as θ_0 .

cloudy conditions, the differences for the two mean-case depending typical ABL types are negligible. The critical value of Ri_{bc} is below 1% and therefore negligible and the mean value of ≈ 0.12 is used for all conditions (with temperature measurements at 2 m height as θ_0).

Bulk Richardson numbers at SML height.

3.4 Surface mixing layer height estimates based on a mean critical Richardson number

To assess the impact of using an averaged critical Ri number on the determination of the individual SML height, we compare h_{Ri_b} to the turbulence-based value h_ϵ . In addition to the tethered balloon profiles, we apply the same surface bulk Richardson number method to the radiosondes profiles using the Met City tower data as a surface reference. Figure 8 shows the comparison of the mixing layer SML heights applying two different Ri_{bc} for both, tethered balloon-borne as well as radiosonde profiles. We use those radiosonde profiles that were launched closest to the tethered balloon flight. In the scatter plots the solid lines are the least squares fits (linear regressions) correspondingly; the statistical measure R^2 (coefficient of determination) and the slope of the fit are printed in the according color. In

For the tethered balloon observations, the slope \bar{h} , using the theoretical value of 0.25 is about 202% higher than when using $Ri_{bc} = 0.12$. As all intercepts are positive, a slope > 1 indicates an overestimation of h . Compared to h_ϵ , h_{Ri_b} with $Ri_{bc} = 0.12$ is about 15% higher while $Ri_{bc} = 0.25$ leads to about 60% overestimation of h . This supports the need of an accurate estimate of Ri_{bc} . Comparison of SML heights: If we apply the newly determined Ri_{bc} and the theoretical value for comparison \bar{h} to the radiosonde observations, the inaccuracies in the determination of h become even more apparent. Besides the slope, also the intercept increases (from 22 with $Ri_{bc} = 0.12$ to 30 with $Ri_{bc} = 0.25$), leading to an overestimation

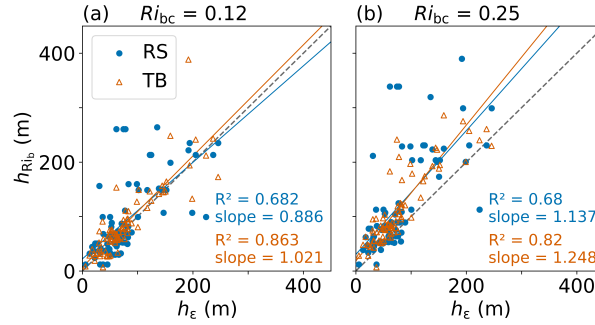


Figure 8. SML height comparisons between the bulk Richardson number approach h_{Ri_b} and turbulence h_ϵ based on tethered balloon (TB, orange) and radiosonde (RS, blue) profiles. For both data sets, two different critical bulk Richardson numbers are used: 0.12 (a), and 0.25 (b). The dashed line represents the 1:1 line. Solid lines are the least squares fits for tethered balloon (orange) and radiosonde (blue) profiles; R^2 and slope values are given for each fit.

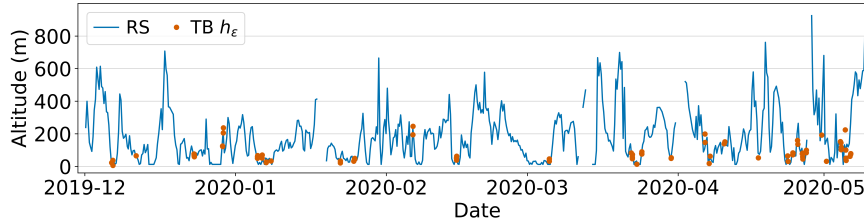


Figure 9. Time series of SML heights from radiosonde data derived with bulk Richardson number method using $Ri_{bc} = 0.12$. The time series of radiosonde launches is displayed between 1 December 2019 and 10 May 2020 (blue). Additionally, the SML heights h_ϵ of tethered balloon borne profiles are shown as orange dots.

of h . It should be noted that the reference altitude-height h_ϵ was not determined exactly at the same time as the height based on the radiosonde ascents.

In a final step Furthermore, we use $Ri_{bc}=0.12$ ~~$Ri_{bc}=0.12$~~ to derive h for all radiosonde launches collected during winter and spring. The Figure 9 shows the time series of the derived SML height is shown in Fig. 9. Additionally, and additionally h_ϵ of the tethered balloon borne turbulence estimates are displayed. balloon-borne turbulence estimates. In Fig. 9-9, a high variability of the SML height is displayed during the entire observation period, reaching from a few tens of meters up to 600 m and more (maximum 925 m). It has to be considered that the minimum detection limit of the radiosonde is of about 12 m due to launching from the helicopter deck. A significant growth of the SML is likely related to weather or storm events, while the SML is shallower for calm or stable conditions. The vast majority (around 81 %) of the SML heights derived from the radiosondes during this period is below 300 m, and around half of the profiles lead to a SML height smaller-less than 150 m.

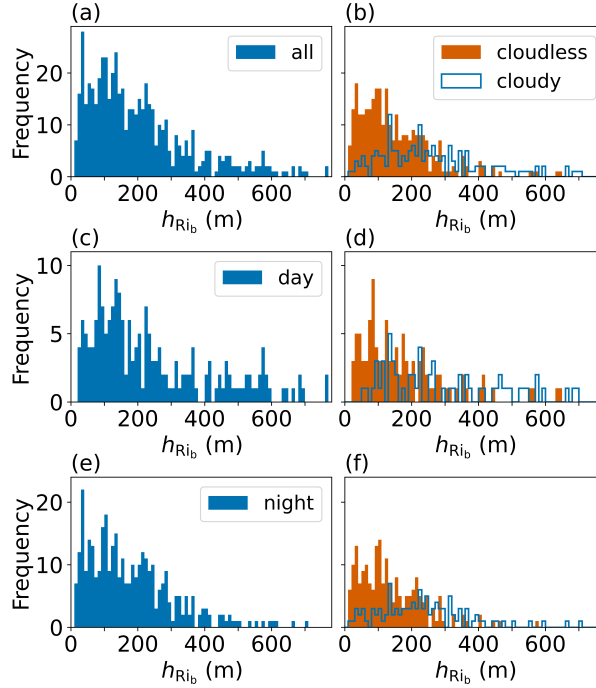


Figure 10. Frequency distribution of SML heights using radiosonde data between 1 December 2019 and 10 May 2020. The radiosonde SML heights are based on bulk Richardson number approach with $Ri_{bc} = 0.12$. The frequency distributions are given for (a) all radiosonde profiles, (b) all data separated according to cloud conditions, (c) all profiles with daylight conditions and (e) all profiles during night, (d) and (f) show the cloudless and cloudy conditions in orange and blue, respectively.

That This shows that even if measurements with the tethered balloon though tethered balloon operations are limited by weather conditions, the tethered balloon measurements can still represent a large part of the SML in this season/time of the year.

Frequency distributions of all derived SML heights using radiosonde data are shown in Fig. 10. During this period the period considered in this plot, the majority of all SML heights is clearly the SML heights are below 250 m (Fig. 10a). Separating between cloudless and cloudy conditions shows that SML heights are spread rather equally between all heights for cloudy conditions, but are significantly smaller for cloudless conditions (Fig. 10b). During daylight conditions (Fig. 10c and d), less cloudless profiles are measured but the distribution is similar, however the lowest SML heights are measured under cloudless conditions. However, the number of profiles with daylight is smaller than during night conditions for our period of analysis daylight profiles is lower than the number of night profiles for our analysis period. Distributions of the SML heights during polar night are shown in Fig. 10e for all conditions, and separately separated by cloud conditions in Fig. 10f. We see that the majority of cloudless conditions lead to SML heights of maximum a maximum of 100 to 200 m, while cloudy conditions do not show any tendency towards a distinct SML height. This distribution shows the variety of clouds and their respective influence on the SML.

405 3.5 Surface mixing layer height estimates based on Monin-Obukhov scaling

Under stable conditions ($B_s < 0$ and $L > 0$), we apply the surface ~~flux-based alternative~~ flux-based method introduced in Sect. 2.2.3 to determine the ~~mixing-layer~~ SML height h_{MO} based on Monin-Obukhov (~~MO~~) similarity scaling. The two covariances underlying the definition of L are estimated from ultrasonic anemometer/thermometer observations from the *Met City* tower ~~in at~~ 2 m height. A running average ($\tilde{x}(t)$) with a centered window over 5 minutes is applied to define the time series of
 410 the fluctuating part as $x'(t) = x(t) - \tilde{x}(t)$ where $\langle x'(t) \rangle = 0$ is fulfilled and x is one of the velocity components (~~u, v, w~~ u, v, w) or virtual temperature T_v (actually, an ultrasonic thermometer measures the ~~so-called~~ so-called "sonic temperature" which differs only very slightly from the virtual temperature at ~~the low humidifies~~, respectively low humidity values). The averaging to calculate the kinematic fluxes leading to L and, finally, h_{MO} is done over 30 minutes centered around the balloon ascents/descents.

415 Figure 11 shows ~~the time series of~~ h_{MO} (Fig. 11a) including h_ε as reference ~~and the Monin-Obukhov length~~ L (Fig. 11b). ~~The 11a) and the~~ net radiation F_{net} ~~is shown in~~ (Fig. 11e), ~~11b) with~~ a threshold of ~~separates~~ -25 W m^{-2} separating cloudless from cloudy conditions.

~~Figure 11 shows that~~ This plot shows a qualitative agreement between h_{MO} and h_ε for cases with two or more subsequent values with $F_{\text{net}} < -25 \text{ W m}^{-2}$, ~~which cover longer lasting cloudless cases, there is a high qualitatively agreement between~~ h_{MO} and h_ε . ~~This holds particular~~ -25 W m^{-2} covering longer-lasting cloudless cases. That is particularly true for the polar night and twilight periods. However, h_{MO} is often slightly lower than h_ε . To determine the scaling height, we averaged over 30 minutes, thus comparing 30-minute statistics with a "snapshot" of the atmosphere. We have tested shorter averaging periods (5 minutes) for profiles 6, 15, and 48. However, this does not explain all discrepancies between the two heights, so we assume that the variations between h_{MO} and h_ε are more likely to indicate atmospheric conditions. Nevertheless, h_{MO} represents the SML
 425 height well during wintertime and cloudless conditions.

In contrast, for profiles 11 to 14 on 29 December 2019 (~~profile numbers 13 to 16~~ period I in Fig. 11, cf. Fig. 3), we find $F_{\text{net}} > -25 \text{ W m}^{-2}$ describing a more cloudy situation with increasing F_{net} . At the beginning of this cloudy period, we ~~find~~ observe a reasonable agreement between h_{MO} and h_ε , but eventually, with further increasing F_{net} , L becomes negative, and MO theory fails to predict ~~a an~~ SML height. Therefore, ~~in situations~~ with rapidly changing cloud cover, SML height determinations
 430 using MO theory are only partially successful ~~and~~. F_{net} observations can at least indicate these possible problems if no vertical profiles of thermodynamic or turbulent parameters are available.

During a short period on 6 February 2020 ~~with two profiles (32 and 33~~ (profiles 30 and 31, period II), a situation with ~~obvious~~ an apparent disagreement between h_{MO} and h_ε but $F_{\text{net}} < -25 \text{ W m}^{-2}$ and L being positive has been identified. This cloudless period was influenced by ~~a LLJ adding a further an LLJ, which added another~~ source of turbulent kinetic energy well above
 435 the surface. The resulting profile of ε , therefore, never falls below the threshold for h_ε between the core of the LLJ and the surface ~~suggesting a SML height much higher compared to~~, indicating a much higher SML height than h_{MO} .

~~In the context of clouds, there is another special situation that can be misinterpreted. Shallow ground fog within a neutrally layered SML up to about~~, capped by an inversion as observed in late March (profile number 46 to 51). The fog was optically

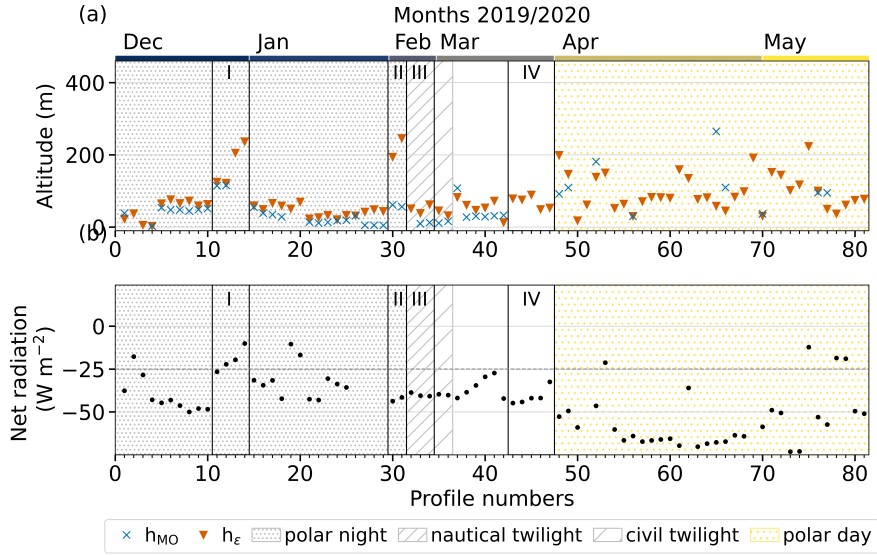


Figure 11. SML heights (a) estimated based on MO sealing method (h_{MO}) and direct in situ turbulence profiles (h_ϵ) as a function of profile number, and (b) the net radiation F_{net} as observed at the surface. Additionally to the profile numbers, the respective month of the year is indicated at the top axis in (a). Further, shading refers to similar to daylight conditions. Periods discussed in the text are marked by bounding and enumerated with roman numbers.

quite thin, associated with F_{net} around -25 W m^{-2} . Due to the elevated inversion, the turbulence threshold value was reached below 100 m . MO theory failed to predict a SML height because $L < 0$.

With the beginning of the twilight (15 February 2020, profile numbers profiles 34 to 36, period III), the cloudless ABL was characterized by a surface inversion and a second an elevated inversion above with, separated by a weakly stable to neutral stratified layer in between. Below the elevated inversion, ϵ was always slightly above the threshold for h_ϵ , suggesting at least some vertical turbulent mixing. However, h_{MO} significantly underestimates the SML height under those conditions.

In the context of clouds, another particular situation may cause misinterpretation. Shallow ground fog within a neutrally stratified SML up to about 45 m capped by an inversion was observed in late March (profiles 46 to 51, period IV). The fog was optically quite thin, associated with $F_{net} < -25 \text{ W m}^{-2}$. Due to the elevated inversion, the turbulence threshold was exceeded below 100 m . MO theory failed to predict an SML height because $L < 0$.

The situation becomes even more complicated in the transition to the polar day when the thermal stratification changes from rather stable to neutral or unstable, and the cloud situation - even with some foggy days - often becomes very complex. This becomes especially clear. These conditions pose challenges for the MO method, especially at the end of the observation period when L is often negative and thus no SML height can be determined based on MO theory.

4 Summary and Conclusion

4 Summary and conclusion

455 This work investigates methods to determine the SML height under different ABL conditions as observed during wintertime and early spring. The main focus of this study is the evaluation of different methods for determining the surface mixing layer (SML) height for typical conditions observed in the central Arctic during MOSAiC. The quantitative identification of the SML height is of considerable significance with regard to the vertical distribution of aerosol particles, clouds and trace gases, as well as cloud formation and decay and precipitation and energy flux processes. For our analysis we have used tethered balloon
460 borne profile measurements of mean and turbulence parameters accompanied by radiosondes and tower based turbulence observations.

Two typical cases in winter and early spring. The two typical observed conditions - cloudless with a surface near-surface temperature inversion and cloudy with a capping an elevated inversion at the cloud top - were observed and analyzed in detail. Our turbulence measurements allowed direct estimates. Further, the applicability of the different SML height determinations
465 was investigated for both conditions individually since they offer partly fundamentally different preconditions.

A major advantage of our dataset is the high-resolution turbulence measurements, which allow direct estimations of the SML height based on a turbulence threshold that is independent of assumptions on stratification or sources of under the basic assumption that the turbulent mixing. With help of this reference height, originating from the surface ends at the height where the turbulence falls below a certain threshold, and the flow thus becomes quasi-laminar. Since this transition from a turbulent
470 to an almost laminar layer occurs quite suddenly, this method is relatively robust concerning the choice of the threshold. This method is not based on any further assumptions and, thus, is used here as a reference method.

This reference height was used to apply the surface bulk Richardson number method was applied and the critical derive the critical value Ri_{bc} , necessary for further SML height estimates, was derived for the condition for the conditions observed during winter and spring of MOSAiC.

475 It was found that differences in an average value of $Ri_{bc} = 0.12$ can be recommended. We also derived Ri_{bc} for individually for the two ABL conditions (cloudless and cloudy conditions can be neglected and a common value of $Ri_{bc} = 0.12$ can be recommended under most conditions. Using the Ri method and the), while the differences between these values are minimal (about 7 % deviation) and hence negligible. That we did not observe a difference in the critical bulk Richardson number for the two cases may be somewhat surprising at first glance since the sources of turbulence are different. For the cloudless case
480 we have mainly the shear-induced turbulence at the surface whereas for the cloudy conditions, turbulence from the cloud top is added, and both overlap. It should be taken into account that we have only determined one term of the energy balance equation with the measured energy dissipation, and, therefore, we cannot make any further statement about the spatial distribution of the turbulent kinetic energy, its sources, or vertical transport. This analysis would require much more complex measurements including the precise three-dimensional wind vector for covariance measurements, which was not the intention of this work. As
485 long as the conditions as described by the (bulk) Richardson number are sufficient for the existence (or generation/suppression) of turbulence ($Ri_b < Ri_{bc}$), the cause for turbulence generation is irrelevant. Thus, the independence of the observed Ri_{bc} value

determined in this work, regular radiosonde ascents provide from turbulence generation in both cases (cloudy and cloudless ABL) is physically reasonable.

One of the main advantages of this work is that the Ri_{bc} method can be applied directly to the regularly performed radiosonde ascents with the determined value $Ri_{bc} = 0.12$. This approach provides reliable estimates of the SML when direct determinations using turbulence profiles height that are about 40 % lower compared to using the canonical value of $Ri_{bc} = 0.25$ ($\langle h_{Ri_{bc}=0.25} / h_{Ri_{bc}=0.12} \rangle = 1.407$). This advantage is particularly important when turbulence measurements from the balloon are not available. Finally, another method for SML height determination based on near surface turbulent fluxes (Monin-Obukhov method) was compared to the reference method and its limitations were investigated due to weather or other reasons.

All methods have advantages and disadvantages. We conclude that without extensive vertical measurements of both mean and turbulent parameters, limitations in some methods may not be detected at all. This leads to There are, of course, other limitations to this study that need to be considered when interpreting the results. For example, we were not able to observe cases of de-coupled cloud situations, which are often observed during the Arctic summer and could change the results. This raises the question of whether the often weak inversion, de-coupling the following specific conclusions: sub-cloud layer from the surface layer, is sufficient to push the turbulence below the threshold value and thus to define the SML height and the height at which Ri_{bc} is determined. The answer to this question urgently requires comparable measurements in the Arctic summer, where these cases are more frequently observed.

There is some confusion in literature about the observed variability. Since the balloon-borne turbulence profiles are not continuously available, this does not allow for an adequate investigation of evolution of the SML height. For this reason, we investigated the applicability of Monin-Obukhov scaling (MO) theory to estimate the SML height. Applying MO to near-surface turbulent flux measurements from tower-based observations, SML heights can be estimated under certain assumptions and compared with the reference heights. Especially for the wintertime, when stable and cloudless conditions prevail, the MO method nicely complements the ABL characterization and provides reliable SML heights. Since the MO method is not applicable for additional sources of turbulence above the surface, such as cloud top cooling or wind shear caused by LLJs, these limitations must be excluded by appropriate observations. Here, at least additional radiosondes are essential for an assessment, while determining surfaces fluxes alone would often lead to erroneous estimates of the SML height for our observations.

Another point to be considered is the sensitivity of Ri_{bc} , which is probably caused by the usage of different definitions of Ri , such as the classical gradient Ri number versus the different bulk approaches. It was argued that the critical values vary less within an experiment than between different experiments. Since we did not find a significant difference in Ri_{bc} for cloudless and cloudy conditions, this hints to on the selection of the different methods as the main cause of this issue lowest observation level. While the mean Ri_{bc} is 0.12 in this study for a 2 m temperature as the surface reference level, Ri_{bc} increases to 0.16 when the skin temperature is used as the surface level temperature. Therefore, values taken from the literature should always be interpreted taking into account with the specifics of the approach applied. Turbulence profiles are eminent in determining applied approach taken into account.

Since Ri_{bc} and should serve as a reference for determining the height of the SML does not seem to be universal for all field experiments and we do not yet know the exact cause for the sometimes considerable variability described in the literature,

it will probably be necessary in the future either to determine Ri_{bc} individually for each experiment or to measure the SML height directly using turbulence measurements.

Under certain conditions Monin-Obukhov theory provides reliable SML heights. However, if only turbulence measurements at the surface are available phenomena such as LLJ cannot be unambiguously detected. Here, at least radiosondes are essential for an assessment. It should be noted that in the Arctic the occurrence of LLJs is very common (?).

Unfortunately, our observations cannot answer other important questions such as the temporal evolution of the SML height during the transition from cloudless to cloudy conditions and vice versa, because we do not have continuous observations during such an ABL evolution. A height estimation using the MO method is no longer applicable here due to the influence of the cloud. Furthermore, the time resolution of the profiling was insufficient to study the important transition processes between cloudless and cloudy conditions. The question remains, how quickly the SML height changes during the polar night when clouds move in or whether those processes are related to local forcing or advection.

Data Availability

All balloon borne data and radiosonde data are available on PANGAEA (Akansu et al., 2021; ?, Maturilli et al., 2022). Surface based tower measurements are available on the Arctic Data Center (Cox et al., 2021) and Cloudnet data can be found here: CLU, 2023: <https://hdl.handle.net/21.12132/2.b697d787e83344ee> gap between consecutive balloon profiles was too large to observe this transition in detail. The latter holds for the tethered balloon turbulence profiles and even more for the radiosonde observations. Ultimately, we believe that only continuous turbulence profile measurements with an optimized measurement strategy can help answer such questions.

Author contribution

H.S. designed the turbulence probe. H.S., S.D., and M.W. contributed to the data analysis and scientific discussion. E.A. processed the data and drafted the manuscript. Finally, we come to the conclusion that turbulence profile measurements are the most reliable method to determine the SML height, but at least profile measurements with radiosondes are necessary to either determine the SML height using the Richardson approach or to check the boundary conditions in combination with MO theory.

Competing interests

The authors declare that they have no competing interests.

Acknowledgements

Data availability. All tethered balloon-borne data (Akansu et al., 2023b, in preparation) and radiosonde data (Maturilli et al., 2022), as well as the 360° photographs (Engelmann et al., 2022, 2023a, b) and total sky imager observations (Nicolaus et al., 2021) are available on PANGAEA. Surface based tower measurements are available on the Arctic Data Center (Cox et al., 2023).

Author contributions. H.S. designed the turbulence probe. H.S., S.D., and M.W. contributed to the data analysis and scientific discussion. E.A. processed the data and prepared the manuscript with contributions from all co-authors.

Competing interests. The authors declare that they have no conflict of interest.

Acknowledgements. We gratefully acknowledge the funding by the Deutsche Forschungsgemeinschaft (DFG, German Research Foundation) – project number 268020496 – TRR 172, within the Transregional Collaborative Research Center “Arctic Amplification: Climate Relevant Atmospheric and Surface Processes, and Feedback Mechanisms (AC³”) in sub project A02. Data used in this manuscript were produced as part of the international Multidisciplinary drifting Observatory for the Study of the Arctic Climate (MOSAiC) with the tag MOSAiC20192020 and the Project_ID: AWI_PS122_01, AWI_PS122_02, AWI_PS122_03. Here, our special thanks go to A. Sommerfeld, J. Gräser and R. Jaiser from the Alfred Wegener Institute who performed the balloon measurements during the first three legs. Tower based measurements were made by the University of Colorado / NOAA surface flux team supported by National Science Foundation (OPP-1724551). Surface radiation measurements were provided by the Atmospheric Radiation Measurement (ARM) User Facility, a U.S. Department of Energy (DOE) Office of Science User Facility Managed by the Biological and Environmental Research Program. Radiosonde data were obtained through a partnership between the leading Alfred Wegener Institute (AWI), the atmospheric radiation measurement (ARM) user facility, a US Department of Energy facility managed by the Biological and Environmental Research Program, and the German Weather Service (DWD). Finally, we thank O. Persson and M. Shupe for fruitful and stimulating discussions on the Arctic atmospheric boundary layer.

References

- Achtert, P., Brooks, I. M., Brooks, B. J., Moat, B. I., Prytherch, J., Persson, P. O. G., and Tjernström, M.: Measurement of wind profiles by motion-stabilised ship-borne Doppler lidar, *Atmos. Meas. Tech.*, 8, 4993–5007, <https://doi.org/10.5194/amt-8-4993-2015>, 2015.
- Akansu, E. F., Siebert, H., Dahlke, S., Graeser, J., Jaiser, R., and Sommerfeld, A.: Tethered balloon-borne measurements of turbulence during the MOSAiC expedition from December 2019 to May 2020, *PANGAEA*, <https://doi.org/10.1594/PANGAEA.932007>, 2021.
- Akansu, E. F., Siebert, H., Dahlke, S., Graeser, J., Jaiser, R., and Sommerfeld, A.: Tethered Balloon-Borne Turbulence Measurements in Winter and Spring during MOSAiC, [accepted] *Sci Data*, 2023a.
- Akansu, E. F., Siebert, H., Dahlke, S., Graeser, J., Jaiser, R., and Sommerfeld, A.: Tethered balloon-borne measurements of turbulence during the MOSAiC expedition from December 2019 to May 2020, [in preparation] *PANGAEA* [data set], 2023b.
- Andreas, E. L., Claffy, K. J., and Makshtas, A. P.: Low-Level Atmospheric Jets And Inversions Over The Western Weddell Sea, *Boundary Layer Meteorol.*, 97, 459–486, <https://doi.org/10.1023/A:1002793831076>, 2000.
- Balsley, B. B., Frehlich, R. G., Jensen, M. L., and Meillier, Y.: High-Resolution In Situ Profiling through the Stable Boundary Layer: Examination of the SBL Top in Terms of Minimum Shear, Maximum Stratification, and Turbulence Decrease, *J. Atmos. Sci.*, 63, 1291–1307, <https://doi.org/10.1175/JAS3671.1>, 2006.
- Becker, R., Maturilli, M., Philipona, R., and Behrens, K.: In situ sounding of radiative flux profiles through the Arctic lower troposphere, *Bull. of Atmos. Sci. & Technol.*, 1, 155–177, <https://doi.org/10.1007/s42865-020-00011-8>, 2020.
- Bintanja, R., Graverson, R. G., and Hazeleger, W.: Arctic winter warming amplified by the thermal inversion and consequent low infrared cooling to space, *Nat. Geosci.*, 4, 758–761, <https://doi.org/10.1038/ngeo1285>, 2011.
- Brooks, I. M., Tjernström, M., Persson, P. O. G., Shupe, M. D., Atkinson, R. A., Canut, G., Birch, C. E., Mauritsen, T., Sedlar, J., and Brooks, B. J.: The Turbulent Structure of the Arctic Summer Boundary Layer During The Arctic Summer Cloud-Ocean Study, *J. Geophys. Res.-Atmos.*, 122, 9685–9704, <https://doi.org/10.1002/2017JD027234>, 2017.
- Cohen, J., Zhang, X., Francis, J., Jung, T., Kwok, R., Overland, J., Ballinger, T. J., Bhatt, U. S., Chen, H. W., Coumou, D., Feldstein, S., Gu, H., Handorf, D., Henderson, G., Ionita, M., Kretschmer, M., Laliberte, F., Lee, S., Linderholm, H. W., Maslowski, W., Peking, Y., Pfeiffer, K., Rigor, I., Semmler, T., Stroeve, J., Taylor, P. C., Vavrus, S., Vihma, T., Wang, S., Wendisch, M., Wu, Y., and Yoon, J.: Divergent consensus on Arctic amplification influence on midlatitude severe winter weather, *Nat. Clim. Chang.*, 10, 20–29, <https://doi.org/10.1038/s41558-019-0662-y>, 2020.
- Cox, C., Gallagher, M., Shupe, M., Persson, O., Solomon, A., Blomquist, B., Brooks, I., Costa, D., Gottas, D., Hutchings, J., Osborn, J., Morris, S., Preusser, A., and Uttal, T.: 10-meter (m) meteorological flux tower measurements (Level 1 Raw), Multidisciplinary Drifting Observatory for the Study of Arctic Climate (MOSAiC), central Arctic, October 2019 - September 2020, Arctic Data Center, <https://doi.org/10.18739/A2VM42Z5F>, 2021.
- Cox, C., Gallagher, M., Shupe, M., Persson, O., Blomquist, B., Grachev, A., Riihimäki, L., Kutchenreiter, M., Morris, V., Solomon, A., Brooks, I., Costa, D., Gottas, D., Hutchings, J., Osborn, J., Morris, S., Preusser, A., and Uttal, T.: Met City meteorological and surface flux measurements (Level 2 Processed), Multidisciplinary Drifting Observatory for the Study of Arctic Climate (MOSAiC), central Arctic, October 2019 - September 2020., Arctic Data Center [data set], <https://doi.org/10.18739/A2TM7227K>, 2023.
- Dai, C., Wang, Q., Kalogiros, J. A., Lenschow, D. H., Gao, Z., and Zhou, M.: Determining Boundary-Layer Height from Aircraft Measurements, *Boundary Layer Meteorol.*, 152, 277–302, <https://doi.org/10.1007/s10546-014-9929-z>, 2014.

- Egerer, U., Gottschalk, M., Siebert, H., Ehrlich, A., and Wendisch, M.: The new BELUGA setup for collocated turbulence and radiation measurements using a tethered balloon: first applications in the cloudy Arctic boundary layer, *Atmos. Meas. Tech.*, 12, 4019–4038, <https://doi.org/10.5194/amt-12-4019-2019>, 2019.
- 605 Engelmann, R., Griesche, H., Radenz, M., Hofer, J., Althausen, D., Macke, A., and Hengst, R.: Total Sky Imager observations during POLARSTERN cruise PS122/1, Tromsø to the northern part of the Arctic Ocean, PANGAEA [data set], <https://doi.org/10.1594/PANGAEA.952150>, 2022.
- Engelmann, R., Griesche, H., Radenz, M., Hofer, J., Althausen, D., Macke, A., and Hengst, R.: Total Sky Imager observations during POLARSTERN cruise PS122/2, Arctic Ocean to Arctic Ocean, PANGAEA [data set], <https://doi.org/10.1594/PANGAEA.954038>, 2023a.
- 610 Engelmann, R., Griesche, H., Radenz, M., Hofer, J., Althausen, D., Macke, A., and Hengst, R.: Total Sky Imager observations during POLARSTERN cruise PS122/3, Arctic Ocean - Longyearbyen, PANGAEA [data set], <https://doi.org/10.1594/PANGAEA.954218>, 2023b.
- Esau, I. and Zilitinkevich, S.: On the role of the planetary boundary layer depth in the climate system, *Adv. Sci. Res.*, 4, 63–69, <https://doi.org/https://doi.org/10.5194/asr-4-63-2010>, 2010.
- Frehlich, R., Meillier, Y., Jensen, M. L., and Balsley, B.: Turbulence Measurements with the CIRES Tethered Lifting System during CASES-99: Calibration and Spectral Analysis of Temperature and Velocity, *J. Atmos. Sci.*, 60, 9, 2003.
- 615 Garratt, J. R.: The atmospheric boundary layer, Cambridge atmospheric and space science series, Cambridge University Press, transferred to digital print. edn., 1997.
- Gierens, R., Kneifel, S., Shupe, M. D., Ebell, K., Maturilli, M., and Löhnert, U.: Low-level mixed-phase clouds in a complex Arctic environment, *Atmos. Chem. Phys.*, 20, 3459–3481, <https://doi.org/https://doi.org/10.5194/acp-20-3459-2020>, 2020.
- 620 Grachev, A. A., Andreas, E. L., Fairall, C. W., Guest, P. S., and Persson, P. O. G.: The Critical Richardson Number and Limits of Applicability of Local Similarity Theory in the Stable Boundary Layer, *Boundary Layer Meteorol.*, 147, 51–82, <https://doi.org/10.1007/s10546-012-9771-0>, 2013.
- Graversen, R. G., Mauritsen, T., Tjernström, M., Källén, E., and Svensson, G.: Vertical structure of recent Arctic warming, *Nature*, 451, 53–56, <https://doi.org/10.1038/nature06502>, 2008.
- 625 Griesche, H. J., Seifert, P., Ansmann, A., Baars, H., Barrientos Velasco, C., Bühl, J., Engelmann, R., Radenz, M., Zhenping, Y., and Macke, A.: Application of the shipborne remote sensing supersite OCEANET for profiling of Arctic aerosols and clouds during *Polarstern* cruise PS106, *Atmos. Meas. Tech.*, 13, 5335–5358, <https://doi.org/10.5194/amt-13-5335-2020>, 2020.
- Griesche, H. J., Ohneiser, K., Seifert, P., Radenz, M., Engelmann, R., and Ansmann, A.: Contrasting ice formation in Arctic clouds: surface-coupled vs. surface-decoupled clouds, *Atmos. Chem. Phys.*, 21, 10357–10374, <https://doi.org/10.5194/acp-21-10357-2021>, 2021.
- 630 Heinemann, G. and Rose, L.: Surface energy balance, parameterizations of boundary-layer heights and the application of resistance laws near an Antarctic Ice Shelf front, *Boundary Layer Meteorol.*, 51, 123–158, <https://doi.org/10.1007/BF00120464>, 1990.
- Illingworth, A. J., Hogan, R. J., O’Connor, E. J., Bouniol, D., Brooks, M. E., Delanoé, J., Donovan, D. P., Eastment, J. D., Gaussiat, N., Goddard, J. W. F., Haefelin, M., Baltink, H. K., Krasnov, O. A., Pelon, J., Piriou, J.-M., Protat, A., Russchenberg, H. W. J., Seifert, A., Tompkins, A. M., Zadelhoff, G.-J. v., Vinit, F., Willén, U., Wilson, D. R., and Wrench, C. L.: Cloudnet: Continuous Evaluation of Cloud Profiles
- 635 in Seven Operational Models Using Ground-Based Observations, *Bull. Amer. Meteor. Soc.*, 88, 883–898, <https://doi.org/10.1175/BAMS-88-6-883>, 2007.
- Intrieri, J. M., Fairall, C. W., Shupe, M. D., Persson, P. O. G., Andreas, E. L., Guest, P. S., and Moritz, R. E.: An annual cycle of Arctic surface cloud forcing at SHEBA, *J. Geophys. Res.*, 107, 8039, <https://doi.org/10.1029/2000JC000439>, 2002a.

- Intrieri, J. M., Shupe, M. D., Uttal, T., and McCarty, B. J.: An annual cycle of Arctic cloud characteristics observed by radar and lidar at SHEBA, *J. Geophys. Res.*, 107, <https://doi.org/10.1029/2000JC000423>, 2002b.
- Jozef, G., Cassano, J., Dahlke, S., and de Boer, G.: Testing the efficacy of atmospheric boundary layer height detection algorithms using uncrewed aircraft system data from MOSAiC, *Atmos. Meas. Tech.*, 15, 4001–4022, <https://doi.org/10.5194/amt-15-4001-2022>, 2022.
- Kitaigorodskii, S. A.: On the computation of the thickness of the wind-mixing layer in the ocean, *Izv. Akad. Nauk Uz SSSR. Ser. Geofiz.*, 3, 425 – 431, 1960.
- Knust, R.: Polar Research and Supply Vessel POLARSTERN Operated by the Alfred-Wegener-Institute, *Journal of large-scale research facilities (JLSRF)*, 3, A119–A119, <https://doi.org/10.17815/jlsrf-3-163>, 2017.
- Lüpkes, C., Vihma, T., Jakobson, E., König-Langlo, G., and Tetzlaff, A.: Meteorological observations from ship cruises during summer to the central Arctic: A comparison with reanalysis data, *Geophys. Res. Lett.*, 37, <https://doi.org/https://doi.org/10.1029/2010GL042724>, 2010.
- Mahrt, L.: Modelling the depth of the stable boundary-layer, *Boundary Layer Meteorol.*, 21, 3–19, <https://doi.org/10.1007/BF00119363>, 1981.
- Maturilli, M., Sommer, M., Holdridge, D. J., Dahlke, S., Graeser, J., Sommerfeld, A., Jaiser, R., Deckelmann, H., and Schulz, A.: MOSAiC radiosonde data (level 3), PANGAEA [data set], <https://doi.org/10.1594/PANGAEA.943870>, 2022.
- Mayfield, J. A. and Fochesatto, G. J.: The Layered Structure of the Winter Atmospheric Boundary Layer in the Interior of Alaska, *J. Appl. Meteor. Climatol.*, 52, 953–973, <https://doi.org/10.1175/JAMC-D-12-01.1>, 2013.
- Morrison, H., de Boer, G., Feingold, G., Harrington, J., Shupe, M. D., and Sulia, K.: Resilience of persistent Arctic mixed-phase clouds, *Nat. Geosci.*, 5, 11–17, <https://doi.org/10.1038/ngeo1332>, 2012.
- Nicolaus, M., Arndt, S., Birnbaum, G., and Katlein, C.: Visual panoramic photographs of the surface conditions during the MOSAiC campaign 2019/20, PANGAEA [data set], <https://doi.org/10.1594/PANGAEA.938534>, 2021.
- Nicolaus, M., Perovich, D. K., Spreen, G., Granskog, M. A., von Albedyll, L., Angelopoulos, M., Anhaus, P., Arndt, S., Belter, H. J., Bessonov, V., Birnbaum, G., Brauchle, J., Calmer, R., Cardellach, E., Cheng, B., Clemens-Sewall, D., Dadic, R., Damm, E., de Boer, G., Demir, O., Dethloff, K., Divine, D. V., Fong, A. A., Fons, S., Frey, M. M., Fuchs, N., Gabarró, C., Gerland, S., Goessling, H. F., Gradinger, R., Haapala, J., Haas, C., Hamilton, J., Hannula, H.-R., Hendricks, S., Herber, A., Heuzé, C., Hoppmann, M., Høyland, K. V., Huntemann, M., Hutchings, J. K., Hwang, B., Itkin, P., Jacobi, H.-W., Jaggi, M., Jutila, A., Kaleschke, L., Katlein, C., Kolabutin, N., Krampe, D., Kristensen, S. S., Krumpen, T., Kurtz, N., Lampert, A., Lange, B. A., Lei, R., Light, B., Linhardt, F., Liston, G. E., Loose, B., Macfarlane, A. R., Mahmud, M., Matero, I. O., Maus, S., Morgenstern, A., Naderpour, R., Nandan, V., Niubom, A., Oggier, M., Oppelt, N., Pätzold, F., Perron, C., Petrovsky, T., Pirazzini, R., Polashenski, C., Rabe, B., Raphael, I. A., Regnery, J., Rex, M., Ricker, R., Riemann-Campe, K., Rinke, A., Rohde, J., Salganik, E., Scharien, R. K., Schiller, M., Schneebeli, M., Semmling, M., Shimanchuk, E., Shupe, M. D., Smith, M. M., Smolyanitsky, V., Sokolov, V., Stanton, T., Stroeve, J., Thielke, L., Timofeeva, A., Tonboe, R. T., Tavri, A., Tsamados, M., Wagner, D. N., Watkins, D., Webster, M., and Wendisch, M.: Overview of the MOSAiC expedition: Snow and sea ice, *Elementa: Science of the Anthropocene*, 10, 000 046, <https://doi.org/10.1525/elementa.2021.000046>, 2022.
- Peng, S., Yang, Q., Shupe, M. D., Xi, X., Han, B., Chen, D., and Liu, C.: Atmospheric boundary layer structure over the Arctic Ocean during MOSAiC, *EGUsphere* [preprint], pp. 1–31, <https://doi.org/10.5194/egusphere-2023-347>, 2023.
- Persson, P. O. G., Fairall, C. W., Andreas, E. L., Guest, P. S., and Perovich, D. K.: Measurements near the Atmospheric Surface Flux Group tower at SHEBA: Near-surface conditions and surface energy budget, *J. Geophys. Res.*, 107, 8045, <https://doi.org/10.1029/2000JC000705>, 2002.

- Rabe, B., Heuzé, C., Regnery, J., Aksenov, Y., Allerholt, J., Athanase, M., Bai, Y., Basque, C., Bauch, D., Baumann, T. M., Chen, D., Cole, S. T., Craw, L., Davies, A., Damm, E., Dethloff, K., Divine, D. V., Doglioni, F., Ebert, F., Fang, Y.-C., Fer, I., Fong, A. A., Gradinger, R., Granskog, M. A., Graupner, R., Haas, C., He, H., He, Y., Hoppmann, M., Janout, M., Kadko, D., Kanzow, T., Karam, S., Kawaguchi, Y., Koenig, Z., Kong, B., Krishfield, R. A., Krumpen, T., Kuhlmei, D., Kuznetsov, I., Lan, M., Laukert, G., Lei, R., Li, T., Torres-Valdés, S., Lin, L., Lin, L., Liu, H., Liu, N., Loose, B., Ma, X., McKay, R., Mallet, M., Mallett, R. D. C., Maslowski, W., Mertens, C., Mohrholz, V., Muilwijk, M., Nicolaus, M., O'Brien, J. K., Perovich, D., Ren, J., Rex, M., Ribeiro, N., Rinke, A., Schaffer, J., Schuffenhauer, I., Schulz, K., Shupe, M. D., Shaw, W., Sokolov, V., Sommerfeld, A., Spreen, G., Stanton, T., Stephens, M., Su, J., Sukhikh, N., Sundfjord, A., Thomisch, K., Tippenhauer, S., Toole, J. M., Vredenburg, M., Walter, M., Wang, H., Wang, L., Wang, Y., Wendisch, M., Zhao, J., Zhou, M., and Zhu, J.: Overview of the MOSAiC expedition: Physical oceanography, *Elementa: Science of the Anthropocene*, 10, 00062, <https://doi.org/10.1525/elementa.2021.00062>, 2022.
- Sedlar, J. and Tjernström, M.: Stratiform Cloud—Inversion Characterization During the Arctic Melt Season, *Boundary Layer Meteorol.*, 132, 455–474, <https://doi.org/10.1007/s10546-009-9407-1>, 2009.
- Serreze, M. C. and Barry, R. G.: Processes and impacts of Arctic amplification: A research synthesis, *Global and Planet. Change*, 77, 85–96, <https://doi.org/10.1016/j.gloplacha.2011.03.004>, 2011.
- Shupe, M. D. and Intrieri, J. M.: Cloud Radiative Forcing of the Arctic Surface: The Influence of Cloud Properties, Surface Albedo, and Solar Zenith Angle, *J. Climate*, 17, 616–628, [https://doi.org/10.1175/1520-0442\(2004\)017<0616:CRFOTA>2.0.CO;2](https://doi.org/10.1175/1520-0442(2004)017<0616:CRFOTA>2.0.CO;2), 2004.
- Shupe, M. D., Persson, P. O. G., Brooks, I. M., Tjernström, M., Sedlar, J., Mauritsen, T., Sjogren, S., and Leck, C.: Cloud and boundary layer interactions over the Arctic sea ice in late summer, *Atmos. Chem. Phys.*, 13, 9379–9399, <https://doi.org/https://doi.org/10.5194/acp-13-9379-2013>, 2013.
- Shupe, M. D., Rex, M., Blomquist, B., Persson, P. O. G., Schmale, J., Uttal, T., Althausen, D., Angot, H., Archer, S., Bariteau, L., Beck, I., Bilberry, J., Bucci, S., Buck, C., Boyer, M., Brasseur, Z., Brooks, I. M., Calmer, R., Cassano, J., Castro, V., Chu, D., Costa, D., Cox, C. J., Creamean, J., Crewell, S., Dahlke, S., Damm, E., de Boer, G., Deckelmann, H., Dethloff, K., Dütsch, M., Ebell, K., Ehrlich, A., Ellis, J., Engelmann, R., Fong, A. A., Frey, M. M., Gallagher, M. R., Ganzeveld, L., Gradinger, R., Graeser, J., Greenamyre, V., Griesche, H., Griffiths, S., Hamilton, J., Heinemann, G., Helmig, D., Herber, A., Heuzé, C., Hofer, J., Houchens, T., Howard, D., Inoue, J., Jacobi, H.-W., Jaiser, R., Jokinen, T., Jourdan, O., Jozef, G., King, W., Kirchgaessner, A., Klingebiel, M., Krassovski, M., Krumpen, T., Lampert, A., Landing, W., Laurila, T., Lawrence, D., Lonardi, M., Loose, B., Lüpkes, C., Maahn, M., Macke, A., Maslowski, W., Marsay, C., Maturilli, M., Mech, M., Morris, S., Moser, M., Nicolaus, M., Ortega, P., Osborn, J., Pätzold, F., Perovich, D. K., Petäjä, T., Pilz, C., Pirazzini, R., Posman, K., Powers, H., Pratt, K. A., Preußner, A., Quéléver, L., Radenz, M., Rabe, B., Rinke, A., Sachs, T., Schulz, A., Siebert, H., Silva, T., Solomon, A., Sommerfeld, A., Spreen, G., Stephens, M., Stohl, A., Svensson, G., Uin, J., Viegas, J., Voigt, C., von der Gathen, P., Wehner, B., Welker, J. M., Wendisch, M., Werner, M., Xie, Z., and Yue, F.: Overview of the MOSAiC expedition: Atmosphere, *Elementa: Science of the Anthropocene*, 10, 00060, <https://doi.org/10.1525/elementa.2021.00060>, 2022.
- Siebert, H., Lehmann, K., and Wendisch, M.: Observations of Small-Scale Turbulence and Energy Dissipation Rates in the Cloudy Boundary Layer, *J. Atmos. Sci.*, 63, 1451–1466, <https://doi.org/10.1175/JAS3687.1>, 2006.
- Solomon, A., Shupe, M. D., Svensson, G., Barton, N. P., Batrak, Y., Bazile, E., Day, J. J., Doyle, J. D., Frank, H. P., Keeley, S., Remes, T., and Tolstykh, M.: The winter central Arctic surface energy budget: A model evaluation using observations from the MOSAiC campaign, *Elementa: Science of the Anthropocene*, 11, 00104, <https://doi.org/10.1525/elementa.2022.00104>, 2023.
- Stramler, K., Genio, A. D. D., and Rossow, W. B.: Synoptically Driven Arctic Winter States, *J. Climate*, 24, 1747–1762, <https://doi.org/10.1175/2010JCLI3817.1>, 2011.

- Stull, R. B.: An introduction to boundary layer meteorology., Kluwer Academic Publishers, The Netherlands, 666 p., 1988.
- 715 Tjernström, M. and Graversen, R. G.: The vertical structure of the lower Arctic troposphere analysed from observations and the ERA-40 reanalysis, *Q.J.R. Meteorol. Soc.*, 135, 431–443, <https://doi.org/10.1002/qj.380>, 2009.
- Turner, D. D., Shupe, M. D., and Zwink, A. B.: Characteristic Atmospheric Radiative Heating Rate Profiles in Arctic Clouds as Observed at Barrow, Alaska, *J. Appl. Meteor. Climatol.*, 57, 953–968, <https://doi.org/10.1175/JAMC-D-17-0252.1>, 2018.
- Vickers, D. and Mahrt, L.: Evaluating Formulations of Stable Boundary Layer Height, *J. Appl. Meteor. Climatol.*, 43, 1736–1749, <https://doi.org/10.1175/JAM2160.1>, 2004.
- 720 Wendisch, M., Macke, A., Ehrlich, A., Lüpkes, C., Mech, M., Chechin, D., Dethloff, K., Velasco, C. B., Brückner, M., Clemen, H.-C., Crewell, S., Donth, T., Dupuy, R., Egerer, U., Engelmann, R., Engler, C., Eppers, O., Gehrman, M., Gong, X., Gourbeyre, C., Griesche, H., Hartmann, J., Hartmann, M., Heinold, B., Herber, A., Herrmann, H., Heygster, G., Hoor, P., Jafariserajehlou, S., Jäkel, E., Jourdan, O., Kästner, U., Kecorius, S., Knudsen, E. M., Köllner, F., Kretzschmar, J., Lelli, L., Leroy, D., Maturilli, M., Mei, L., Mertes, S., Mioche, G., Neuber, R., Nicolaus, M., Nomokonova, T., Notholt, J., Palm, M., van Pinxteren, M., Quaas, J., Richter, P., Ruiz-Donoso, E., Schäfer, M., Schmieder, K., Schnaiter, M., Schneider, J., Schwarzenböck, A., Seifert, P., Shupe, M. D., Siebert, H., Spreen, G., Stapf, J., Vogl, T., Welte, A., Wex, H., Zanatta, M., and Zeppenfeld, S.: The Arctic Cloud Puzzle: Using ACLOUD/PASCAL Multiplatform Observations to Unravel the Role of Clouds and Aerosol Particles in Arctic Amplification, *Bull. Amer. Meteor. Soc.*, 100, 841 – 871, <https://doi.org/https://doi.org/10.1175/BAMS-D-18-0072.1>, 2019.
- 730 Wendisch, M., Brückner, M., Crewell, S., Ehrlich, A., Notholt, J., Lüpkes, C., Macke, A., Burrows, J. P., Rinke, A., Quaas, J., Maturilli, M., Schemann, V., Shupe, M. D., Akansu, E. F., Barrientos-Velasco, C., Bärfuss, K., Blechschmidt, A.-M., Block, K., Bougoudis, I., Bozem, H., Böckmann, C., Bracher, A., Bresson, H., Bretschneider, L., Buschmann, M., Chechin, D. G., Chylik, J., Dahlke, S., Deneke, H., Dethloff, K., Donth, T., Dorn, W., Dupuy, R., Ebell, K., Egerer, U., Engelmann, R., Eppers, O., Gerdes, R., Gierens, R., Gorodetskaya, I. V., Gottschalk, M., Griesche, H., Gryanik, V. M., Handorf, D., Harm-Altstädter, B., Hartmann, J., Hartmann, M., Heinold, B., Herber, A., Herrmann, H., Heygster, G., Höschel, I., Hofmann, Z., Hölemann, J., Hünnerbein, A., Jafariserajehlou, S., Jäkel, E., Jacobi, C., Janout, M., Jansen, F., Jourdan, O., Jurányi, Z., Kalesse-Los, H., Kanzow, T., Käthner, R., Kliesch, L. L., Klingebiel, M., Knudsen, E. M., Kovács, T., Körtke, W., Krampe, D., Kretzschmar, J., Kreyling, D., Kulla, B., Kunkel, D., Lampert, A., Lauer, M., Lelli, L., Lerber, A. v., Linke, O., Löhnert, U., Lonardi, M., Losa, S. N., Losch, M., Maahn, M., Mech, M., Mei, L., Mertes, S., Metzner, E., Mewes, D., Michaelis, J., Mioche, G., Moser, M., Nakoudi, K., Neggers, R., Neuber, R., Nomokonova, T., Oelker, J., Papakonstantinou-Presvelou, I., Pätzold, F., Pefanis, V., Pohl, C., Pinxteren, M. v., Radovan, A., Rhein, M., Rex, M., Richter, A., Risse, N., Ritter, C., Rostosky, P., Rozanov, V. V., Donoso, E. R., Garfias, P. S., Salzmänn, M., Schacht, J., Schäfer, M., Schneider, J., Schnierstein, N., Seifert, P., Seo, S., Siebert, H., Soppa, M. A., Spreen, G., Stachlewska, I. S., Stapf, J., Stratmann, F., Tegen, I., Viceto, C., Voigt, C., Vountas, M., Walbröl, A., Walter, M., Wehner, B., Wex, H., Willmes, S., Zanatta, M., and Zeppenfeld, S.: Atmospheric and Surface Processes, and Feedback Mechanisms Determining Arctic Amplification: A Review of First Results and Prospects of the (AC)³ Project, *Bull. Amer. Meteor. Soc.*, 104, E208–E242, <https://doi.org/10.1175/BAMS-D-21-0218.1>, 2023a.
- 740 Wendisch, M., Stapf, J., Becker, S., Ehrlich, A., Jäkel, E., Klingebiel, M., Lüpkes, C., Schäfer, M., and Shupe, M. D.: Effects of variable ice–ocean surface properties and air mass transformation on the Arctic radiative energy budget, *Atmos. Chem. Phys.*, 23, 9647–9667, <https://doi.org/10.5194/acp-23-9647-2023>, 2023b.
- Wyngaard, J. C.: Turbulence in the atmosphere, Cambridge University Press, 393 p., 2012.
- 750 Zhang, Y., Gao, Z., Li, D., Li, Y., Zhang, N., Zhao, X., and Chen, J.: On the computation of planetary boundary-layer height using the bulk Richardson number method, *Geosci. Model Dev.*, 7, 2599–2611, <https://doi.org/10.5194/gmd-7-2599-2014>, 2014.

Zilitinkevich, S.: On the determination of the height of the Ekman boundary layer., *Boundary Layer Meteorol.*, 3, 141 – 145, 1972.

Zilitinkevich, S. and Baklanov, A.: Calculation Of The Height Of The Stable Boundary Layer In Practical Applications, *Boundary Layer Meteorol.*, 105, 389–409, <https://doi.org/10.1023/A:1020376832738>, 2002.

755 **Appendix A:** [Appendix A](#)

Table A1. Overview of tethered balloon-borne profiles. The profile number, start time, and derived SML heights are given using the direct in situ method (h_ε), the bulk Richardson number approach with the surface temperature at 2 m height and a critical value of $Ri_{bc} = 0.12$ (h_{Ri_b}), and the MO method (h_{MO}).

#	Time (UTC)	h_ε (m)	h_{Ri_b} (m)	h_{MO} (m)	#	Time (UTC)	h_ε (m)	h_{Ri_b} (m)	h_{MO} (m)
1	2019-12-06 12:18:29	22	19	38	42	2020-03-23 12:17:35	13	28	32
2	2019-12-06 18:15:29	37	7		43	2020-03-24 11:44:20	79	81	
3	2019-12-06 18:57:32	6	8		44	2020-03-24 12:47:28	76	86	
4	2019-12-07 06:12:50	3	8	3	45	2020-03-24 13:12:10	89	88	
5	2019-12-11 13:27:46	65	59	54	46	2020-03-30 13:28:35	49	54	
6	2019-12-23 11:10:27	76	59	47	47	2020-03-30 13:56:55	53	56	
7	2019-12-23 11:30:21	66	61	48	48	2020-04-06 12:21:27	199	133	92
8	2019-12-23 11:50:07	73	72	44	49	2020-04-06 12:47:00	147	145	109
9	2019-12-23 12:41:36	59	52	48	50	2020-04-07 09:01:10	18	40	
10	2019-12-23 12:54:10	64	57	51	51	2020-04-07 14:09:33	62	68	
11	2019-12-29 07:50:18	125	129	114	52	2020-04-10 11:33:16	139	142	181
12	2019-12-29 08:05:42	122	146	115	53	2020-04-10 14:26:00	150	146	
13	2019-12-29 11:27:41	205	241		54	2020-04-17 11:55:42	52	74	
14	2019-12-29 11:55:41	237	243		55	2020-04-23 12:31:52	64	34	
15	2020-01-05 11:51:44	59	56	55	56	2020-04-23 14:27:10	30	52	30
16	2020-01-05 12:19:12	49	75	39	57	2020-04-24 13:39:04	71	79	
17	2020-01-05 13:01:29	66	72	35	58	2020-04-24 14:18:55	83	89	
18	2020-01-05 13:17:17	59	70	28	59	2020-04-24 14:47:16	82	96	
19	2020-01-06 10:56:53	51	29		60	2020-04-24 15:00:08	81	95	
20	2020-01-06 11:22:02	70	62		61	2020-04-25 12:58:12	159	248	
21	2020-01-07 07:19:21	23	28	14	62	2020-04-25 14:41:58	135		
22	2020-01-07 07:44:02	27	33	11	63	2020-04-26 12:20:09	77	89	
23	2020-01-08 07:25:12	33	36	13	64	2020-04-26 14:20:25	82	70	
24	2020-01-22 12:59:45	21	32	18	65	2020-04-26 14:44:57	59	62	265
25	2020-01-22 13:17:39	33	32	19	66	2020-04-26 14:56:27	45	60	109
26	2020-01-25 07:23:57	32	44	31	67	2020-04-27 08:30:07	84	110	
27	2020-01-25 11:06:54	42	36	5	68	2020-04-27 08:51:28	99	127	
28	2020-01-25 12:06:00	49	27	5	69	2020-04-30 12:19:58	192	388	
29	2020-01-25 12:24:59	44	28	5	70	2020-05-01 12:06:06	31	73	36
30	2020-02-06 11:19:46	194	194	61	71	2020-05-04 08:40:34	152	164	
31	2020-02-06 11:33:48	246	173	56	72	2020-05-04 11:39:30	144	157	
32	2020-02-15 10:14:20	51	60		73	2020-05-04 12:36:04	102	149	
33	2020-02-15 10:44:14	38	59	9	74	2020-05-04 13:06:24	118	116	
34	2020-02-15 11:04:53	62	62	12	75	2020-05-05 08:46:10	224	212	
35	2020-03-05 12:10:54	45	27	11	76	2020-05-05 11:39:30	100	81	95
36	2020-03-05 12:27:04	32	27	16	77	2020-05-05 12:12:09	50	71	95
37	2020-03-22 08:54:08	82	77	108	78	2020-05-05 12:50:27	37	91	
38	2020-03-22 13:29:02	61	68	27	79	2020-05-06 08:08:55	62	153	
39	2020-03-22 13:54:00	47	64	30	80	2020-05-06 11:42:15	74	94	
40	2020-03-22 14:10:30	53	76	29	81	2020-05-06 12:09:51	78	111	
41	2020-03-22 14:17:36	72	77	31					